Monthly Notices
of the
ROYAL ASTRONOMICAL SOCIETY

MNRAS **452,** 3508–3528 (2015) doi:10.1093/mnras/stv1325

Hierarchical star formation across the ring galaxy NGC 6503

Dimitrios A. Gouliermis,[1,2]★ David Thilker,[3] Bruce G. Elmegreen,[4] Debra M. Elmegreen,[5] Daniela Calzetti,[6] Janice C. Lee,[7]† Angela Adamo,[8] Alessandra Aloisi,[7] Michele Cignoni,[7] David O. Cook,[9] Daniel A. Dale,[9] John S. Gallagher, III,[10] Kathryn Grasha,[6] Eva K. Grebel,[11] Artemio Herrero Davó,[12] Deidre A. Hunter,[13] Kelsey E. Johnson,[14] Hwihyun Kim,[15,16] Preethi Nair,[17] Antonella Nota,[7] Anne Pellerin,[18] Jenna Ryon,[10] Elena Sabbi,[7] Elena Sacchi,[19,20] Linda J. Smith,[21] Monica Tosi,[20] Leonardo Ubeda[7] and Brad Whitmore[7]

Affiliations are listed at the end of the paper

Accepted 2015 June 11. Received 2015 June 11; in original form 2015 May 4

ABSTRACT

We present a detailed clustering analysis of the young stellar population across the star-forming ring galaxy NGC 6503, based on the deep *Hubble Space Telescope* photometry obtained with the Legacy ExtraGalactic UV Survey. We apply a contour-based map analysis technique and identify in the stellar surface density map 244 distinct star-forming structures at various levels of significance. These stellar complexes are found to be organized in a hierarchical fashion with 95 per cent being members of three dominant super-structures located along the star-forming ring. The size distribution of the identified structures and the correlation between their radii and numbers of stellar members show power-law behaviours, as expected from scale-free processes. The self-similar distribution of young stars is further quantified from their autocorrelation function, with a fractal dimension of ∼1.7 for length-scales between ∼20 pc and 2.5 kpc. The young stellar radial distribution sets the extent of the star-forming ring at radial distances between 1 and 2.5 kpc. About 60 per cent of the young stars belong to the detected stellar structures, while the remaining stars are distributed among the complexes, still inside the ring of the galaxy. The analysis of the time-dependent clustering of young populations shows a significant change from a more clustered to a more distributed behaviour in a time-scale of ∼60 Myr. The observed hierarchy in stellar clustering is consistent with star formation being regulated by turbulence across the ring. The rotational velocity difference between the edges of the ring suggests shear as the driving mechanism for this process. Our findings reveal the interesting case of an inner ring forming stars in a hierarchical fashion.

Key words: methods: statistical – stars: formation – galaxies: individual: NGC 6503 – galaxies: spiral – galaxies: stellar content – galaxies: structure.

1 INTRODUCTION

Star formation, the conversion of gas into stars, is a key process in shaping the structure, morphology and evolution of galaxies. Young star clusters, OB associations and large complexes of young stars are the signposts of the recent star formation across a galaxy. These various young stellar concentrations, covering a large dynamic range in physical length-scales, do not appear to be independent from each other but rather related to each other in a hierarchical fashion. Large loose structures of stars host smaller and more compact star-forming systems, which themselves are substructured (e.g. Elmegreen et al. 2000). The characterization of this clustering behaviour and its origins are key issues in understanding how star formation progresses in space and time across galactic scales. Samples of resolved young stellar populations across a whole galaxy allow the detailed investigation of their formation in structures, improving our understanding from integrated stellar light.

There are only a few investigations on the clustering of resolved young stars across galactic scales. They are focused on the

★E-mail: gouliermis@uni-heidelberg.de, dgoulier@mpia.de
†Visiting Astronomer, Spitzer Science Center, Caltech, Pasadena, CA 91125, USA

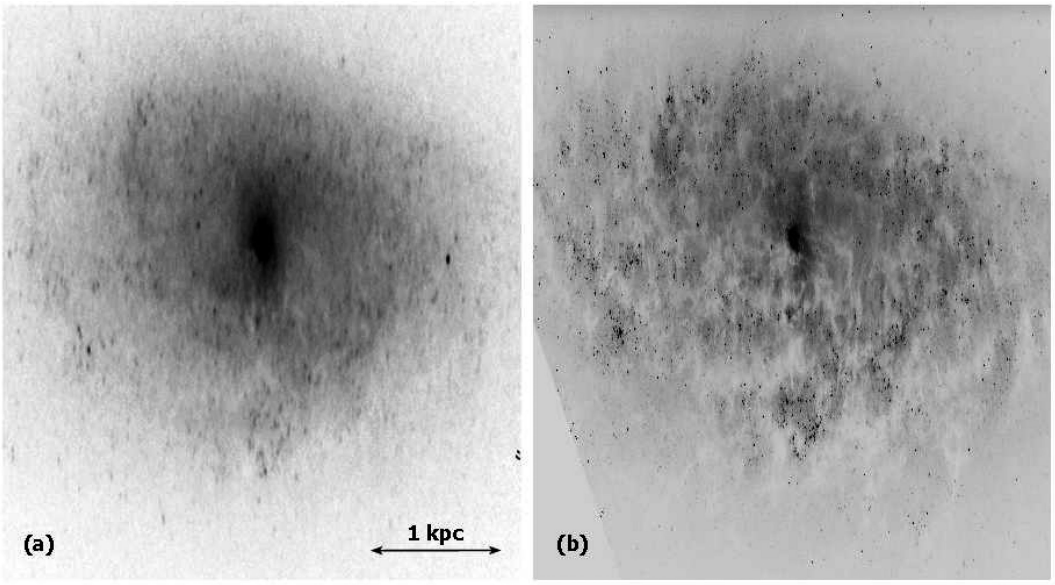

Figure 1. Deprojected images of NGC 6503. (a) Ground-based *H*-band (1.6 μm) image obtained by members of our team with the WHIRC NIR imager at the WIYN 3.5 m telescope. (b) *HST* LEGUS image in the WFC3 filter *F*555*W* (530.8 nm). These images provide evidence for the bar of the galaxy and indicate the overall presence of spiral structure with its weak arms. Details on the deprojection technique are given in Section 2.2.

Magellanic Clouds (Maragoudaki et al. 1998; Gieles, Bastian & Ercolano 2008; Bastian et al. 2009), NGC 6822 (Gouliermis et al. 2010) and M33 (Bastian et al. 2007), up to sub-Mpc distances, where individual stars could be resolved from the ground. These studies give evidence of the self-similar scaling relations in the parameters of the identified stellar structures, demonstrating the hierarchical nature of stellar structural morphology on galactic scales. With the present study, we extend these investigations to larger distances in the Local Volume, based on the exquisite resolving ability of the *Hubble Space Telescope* (*HST*) with its cameras Advanced Camera for Surveys (ACS) and Wide-Field Camera 3 (WFC3). We also add to the sample of investigated galaxies the interesting case of the ring (possibly barred) spiral galaxy NGC 6503 (Fig. 1).

NGC 6503 is classified as of morphological type SAB(s)bc:,[1] i.e. a pure s-shaped spiral galaxy, with possibly well-developed spiral arms, showing a trace of a bar (Buta et al. 2015). The galaxy also has a patchy circumnuclear appearance in Hα, interpreted by Knapen et al. (2006) as a nuclear star-forming ring. The same authors postulate that while this galaxy is possibly one of the rare cases of ring spirals classed as unbarred,[2] it is most likely to actually be barred. Indeed, both the H I velocity field (Bottema & Gerritsen 1997) and near-IR imaging (Freeland et al. 2010) support the presence of a strong end-on bar. Moreover, Freeland et al. (2010) argue that the previously identified nuclear ring is instead an inner ring spanned in diameter by the bar (Fig. 1). According to theory, rings form by gas accumulation through the action of gravitational torques from the bar pattern (e.g. Simkin, Su & Schwarz 1980; Schwarz 1984). They are thus sites of active star formation in the galaxy (Buta & Combes 1996).

Being a ring galaxy observed by *HST*, NGC 6503 is a unique case for investigating in detail star formation across an inner ring. Specific questions that can be probed are: (a) What is the length-scale of stellar structures that can be formed in the ring, and for how long can they survive? (b) Is star formation hierarchical across the ring? (c) What is the role of ring dynamics in the star formation process? In order to answer these questions, we use the rich census of young blue stars resolved with *HST* in NGC 6503, and we investigate their recent star formation as imprinted in their clustering morphology. Our goal is to quantify the young stellar spatial distribution and characterize its clustering on galactic scales, identify any characteristic scale of star formation or confirm its scale-free nature, determine the time-scale for large-scale structure survival and resolve its connection to the dynamics of the galaxy.

Located at a distance of about 5 Mpc (Karachentsev et al. 2003), NGC 6503 is far enough for its entire extent to be mostly covered in a single WFC3 field of view, but also close enough for its young stellar content (down to $\sim$5 $M_\odot$) to be sufficiently resolved with *HST*. The galaxy is also located away from the Galactic plane ($b = 30.^\circ64$) and therefore does not suffer from significant foreground extinction from the Milky Way, which corresponds to a reddening of $E(B-V) \simeq 0.03$ mag (Schlafly & Finkbeiner 2011). With this analysis we demonstrate the great advancement in resolved extra-galactic stellar populations studies, accomplished with the Legacy ExtraGalactic UV Survey[3] (LEGUS), aimed at the investigation of star formation and its relation with galactic environment in 50 nearby star-forming galaxies (Calzetti et al. 2015).

This paper is organized as the following. In Section 2, we describe the LEGUS data set of NGC 6503 and its photometry. We also select the stellar samples corresponding to the young blue populations of the galaxy, and address their spatial distribution in comparison to that of the more evolved populations. In Section 3, we perform

[1] This type is according to the classification by Buta et al. (2015) from the Spitzer Survey of Stellar Structure in Galaxies. The galaxy was previously classified according to the Third Reference Catalog of Bright Galaxies (de Vaucouleurs et al. 1991) as SA(s)cd, i.e. a non-barred spiral with loosely wound spiral arms and with no apparent ring.

[2] Rings are most probably resonance phenomena, caused by a rotating bar or other non-axisymmetric disturbance in the disc. The current evidence supports the idea that 'rings are a *natural* consequence of barred galaxy dynamics' (Buta & Combes 1996).

[3] https://legus.stsci.edu/

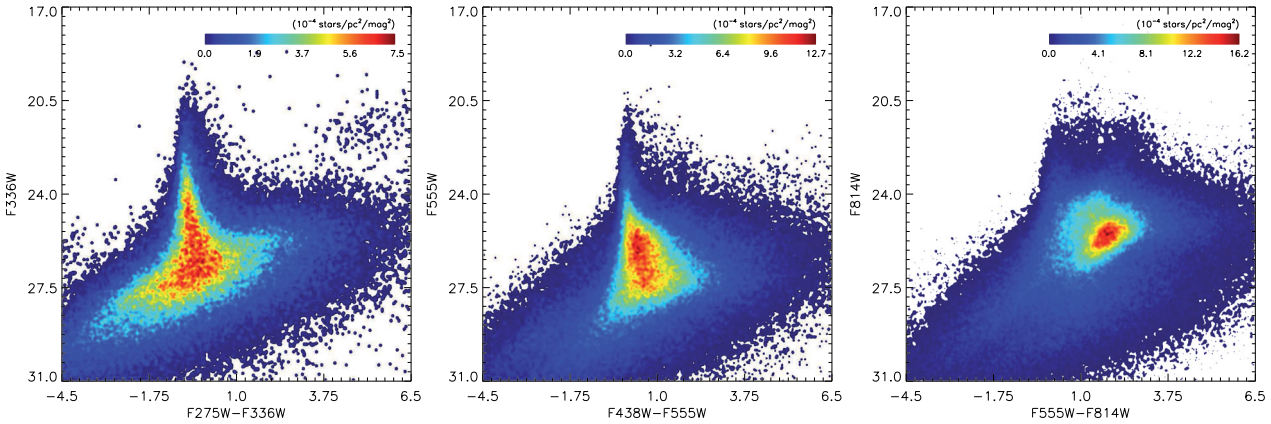

Figure 2. Hess diagrams of the observed stellar populations across the extent of NGC 6503. Three diagrams are shown for stars identified in three different LEGUS filter pairs with no quality cuts. Stellar surface densities across the diagrams are indicated by the colour bars.

the identification of large young stellar structures across the galaxy, and present their structure tree to visualize their hierarchical morphology. In this section, we also discuss the demographics of the structural parameters of the identified systems and investigate their parameter correlations in an attempt to identify any characteristic scale of star formation or the power-law behaviour expected from scale-free processes. In Section 4, we study the global spatial distribution of the stars through their surface density profiles and quantify their hierarchical distribution across the whole galaxy with the construction of their two-point (auto-)correlation function. In the same section, we determine the time-scale for the evolution of stellar structures through the study of the pair separations and the minimum spanning trees (MST) of stars as a function of their indicative evolutionary ages. In Section 5, we discuss our findings in terms of galactic dynamics across the star-forming ring. We summarize our results in Section 6.

2 OBSERVATIONS AND PHOTOMETRY

LEGUS is an *HST* panchromatic stellar survey of 50 nearby star-forming dwarf and spiral galaxies with an emphasis on UV-enabled science applications. Images in a wide waveband coverage from the near-UV (NUV) to the *I* band are being collected with WFC3 and ACS in parallel, and combined with archival optical ACS data. The survey, its scientific objectives and the data reduction are described in Calzetti et al. (2015). Stellar photometry will be described in detail in Sabbi et al. (in preparation). The images of NGC 6503 to be used in our analysis were obtained in the filters *F*275*W*, *F*336*W*, *F*438*W*, *F*555*W* and *F*814*W* (equivalent to NUV, *U*, *B*, *V* and *I*, respectively) in 2013 August. We applied the pixel-based correction for charge-transfer efficiency degradation using tools provided by STScI, before processing them with ASTRODRIZZLE and prior to their photometry.

Photometry was performed with the package DOLPHOT (e.g. Dolphin 2000). This package performs point spread function (PSF) fitting using PSFs especially tailored to *HST* cameras. Before performing the photometry, we first prepared the images using the DOLPHOT packages ACSMASK and SPLITGROUPS. Respectively, these two packages apply the image defect mask and then split the multi-image STScI FITS files into a single FITS file per chip. We then used the main DOLPHOT routine to make photometric measurements in each filter independently of the pre-processed images, relative to the coordinate system of the drizzled reference image. The output photometry from DOLPHOT is on the calibrated VEGAMAG scale based on the zero-points provided on the WFC3 page.[4] Indicative Hess diagrams of the complete stellar samples retrieved with this process are shown in Fig. 2. From these diagrams, it is seen that different wavelengths cover different stellar types, with young stars in the blue filters and old stars in the red filters.

It should be noted that our stellar photometry may include unresolved stellar clusters or multiple systems. However, the criteria applied in the following section for the selection of the best photometric measurements eliminate this contamination to the minimum. In any case, such systems, as well as unresolved binary systems, which should be still included in the best photometric sample, have a negligible effect on our analysis, because the measured blue light of every source is determined by that of the dominant bright star in the system.

2.1 Selection of the stellar sample

We separate the stellar sources with the most reliable photometry into four catalogues, each including stars found in two adjacent filters throughout the complete wavelength coverage from *F*275*W* (UV) to *F*814*W* (*I*). The waveband coverage of the filter pairs overlaps, so that, e.g., the bluer pair (*F*275*W*, *F*336*W*) shares the filter *F*336*W* with the next redder pair (*F*336*W*, *F*438*W*), which shares the filter *F*438*W* with the next and so forth. Since bluer filters cover the younger populations, while the redder ones identify mostly the more evolved stars, our selection distinguishes stars at roughly different evolutionary stages. These *best photometrically defined* stellar samples are determined in terms of quality parameters returned by our photometry. We apply the selection of this sample for stellar sources identified successfully in at least two adjacent filters. We compile the final photometric stellar catalogues in each filter pair by applying the following quality criteria:

DOLPHOT type of the source, TYPE =1;
crowding of the source in each of the filters, CROWD < 2;
sharpness of the source squared in each filter, SHARP^2 < 0.3;
signal-to-noise ratio in each filter, SNR >5.

In DOLPHOT, the object-type parameter has a value of 1 for the best stars in the photometry. Stars too faint for PSF determination and non-stellar sources have TYPE >1. The crowding parameter is a

[4] http://www.stsci.edu/hst/wfc3

Table 1. Statistics on stellar samples with best photometry in various filter pairs. Different stellar samples are coded by different colours, given in column 1, throughout the text.

Sample	Filter pair	Total number of sources	Number of sources not in bluer filters	Percentage over whole sample
Blue	*F*275*W*, *F*336*W*	12 834		
Green	*F*336*W*, *F*438*W*	13 499	1570	12 per cent
Yellow	*F*438*W*, *F*555*W*	21 438	8484	40 per cent
Red	*F*555*W*, *F*814*W*	42 511	27 525	65 per cent

measure of how much brighter the star would have been measured had nearby stars not been fitted simultaneously. For an isolated star, it has the value of zero. The sharpness is zero for a perfectly-fitted star, positive for a star that is too sharp and negative for a star that is too broad.[5]

Statistics on each filter-pair stellar catalogue are given in Table 1. Stellar samples are given a colour name (column 1) based on the wavelength coverage of each filter pair from blue to red (specified in column 2). Column 3 corresponds to the numbers of all stars found in the specific filter pair, including sources also detected in the bluer filter pair. We count how many more stars we detect in every redder filter pair by selecting those stars that have not been identified in the bluer filter pairs, and in column 4 we provide the corresponding numbers of these 'additional' stars. The corresponding percentages over the total numbers of stars in every filter pair are given in column 5 of Table 1.

Indicative Hess diagrams of the blue (filter pair *F*275*W*, *F*336*W*), yellow (*F*438*W*, *F*555*W*) and red (*F*555*W*, *F*814*W*) stellar samples are shown in Figs 3, 4 and 5, respectively. In the case of the two latter pairs, we show the Hess diagrams of both the complete stellar samples (left-hand panels of Figs 4 and 5) and the stars remaining in the catalogues after subtracting those that have also been identified in the bluer filter pairs (right-hand panels of the figures). It is shown that after this subtraction, the majority of the main-sequence (MS) population is almost entirely eliminated in both diagrams, indicating more clearly that they correspond mostly to evolved stellar populations. Small contamination of the blue-faint part of these diagrams by residual MS stars is expected due to the deeper observations in the corresponding filters in comparison to the blue filters and due to photometric uncertainties.

The comparative study of different stellar samples, as selected above, allows us to investigate the differences in the clustering behaviour between stars that correspond to different evolutionary stages, from the most recent star formation events to those corresponding to earlier stellar generations in NGC 6503. Our investigation deals with the clustering behaviour of the most recent stellar generation in the galaxy, i.e. the blue sample (Fig. 3), but for comparison we also address the distribution of the general population of NGC 6503, by considering stars detected in the red sample (Fig. 5 – right-hand panel). Indeed, stars in these two evolutionary stages demonstrate different distributions across the observed field of view. This is shown, for example, in the map of the stars in the blue sample (found in the *F*275*W* and *F*336*W* filters) and that of the red stellar sample (found in the *F*555*W* and *F*814*W* filters), displayed in Fig. 6 (top panel). The young blue stars appear to populate more

[5] More details about the fit-quality parameters are given in DOLPHOT documentation, available at http://americano.dolphinsim.com/dolphot/

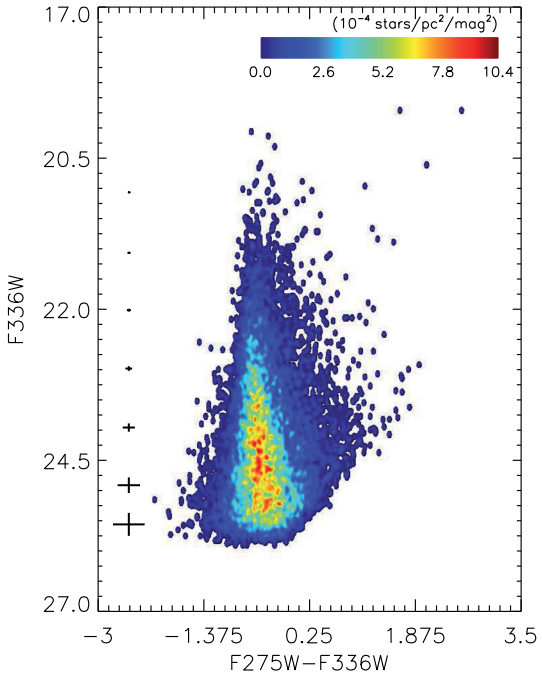

Figure 3. Hess diagram of stars identified in NGC 6503 with the best photometric quality (see Section 2.1) in the LEGUS filter pair *F*275*W*, *F*336*W*. Stellar surface densities across the Hess diagrams are indicated by the colour bars. Crosses on the left represent typical photometric uncertainties. This sample, corresponding to the most recently formed stars in NGC 6503, is the 'blue' sample in our analysis.

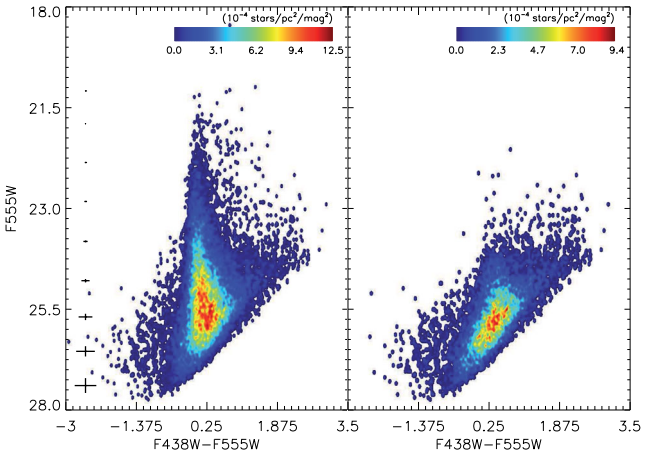

Figure 4. As in Fig. 3 for the stars identified with the best photometric quality in the LEGUS filter pair *F*438*W*, *F*555*W*. Left-hand panel: the Hess diagram of *all* stars detected in this filter pair. Right-hand panel: the Hess diagram of the remaining sources found *only* in *F*438*W* and *F*555*W* after excluding those also observed in the *F*275*W*, *F*336*W* filter pair. There is only a small fraction of main-sequence stars included in this diagram, remained due to the longer exposures in these filters than in *F*275*W* and *F*336*W*.

well-defined structures, while the red population is much more extended, populating the whole observed disc of the galaxy.

We compared these distributions against the light distribution from *Spitzer* images from Dale et al. (2009) in 4.5 μm, tracing old stars, and 8 μm, an indicator based on dust emission of where the young stars are, in order to check whether the observed stellar distributions could be affected by dust attenuation. This comparison confirmed that the blue stars are more clustered in a ring-like

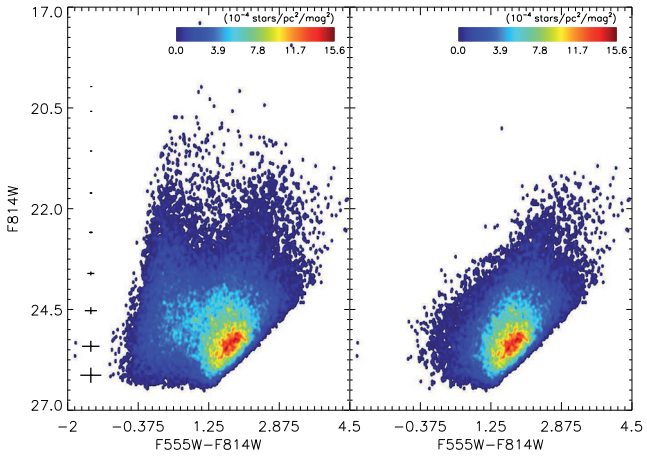

Figure 5. As in Fig. 4 for the stars identified with the best photometric quality in the LEGUS filter pair *F*555*W*, *F*814*W*. Hess diagrams are shown for stars detected *also* in the bluer filters (*F*275*W*, *F*336*W*, *F*438*W*; left-hand panel), as well as for those found *only* in the two considered bands (right-hand panel). Fainter main-sequence stars, which remained after the subtraction of sources also identified in the *F*275*W* and *F*336*W* filters, can be seen in the sample on the right. This residual population persisted due to the longer exposures in the optical filters than in the UV filters. The vast majority of the sources in the diagram in the right-hand panel represents stars at later evolutionary stages. This is the 'red' stellar sample in our analysis.

structure, traced by the 8 μm image, while the 4.5 μm image shows a smooth distribution for the old populations.[6] Nevertheless, the distributions shown in Fig. 6 (top panel) suffer from projection effects that limit our analysis on the global stellar clustering through the observed stellar distributions. Thus, we correct the observed stellar positions for the known inclination of the galaxy.

2.2 Correction for projection of the galactic disc

In order to assess the spatial distribution of stars, free from the effect of projection of the galactic disc, we apply a deprojection of the stellar positions from the plane of the sky to the plane of the galaxy, under the simple assumption of an axisymmetric flat rotating disc for NGC 6503. This assumption is based on the remarkably regular gas kinematics in NGC 6503 that are well described by rotation only (Kuzio de Naray et al. 2012).

For a star with position (x, y) in the plane of the sky (where the centre of the galaxy is at the origin), a simple rotation by the position angle, ϕ, yields

$$\begin{aligned} x' &= x\sin(\phi) - y\cos(\phi) \\ y' &= x\cos(\phi) + y\sin(\phi). \end{aligned} \quad (1)$$

The coordinates of the star in the mid-plane of the galaxy are then x' and $y'/\cos(i)$, i being the inclination angle. We rotated our stellar catalogues for a position angle of $\phi = 135^\circ$, determined by the orientation of the observed field of view. We then corrected them for projection for an inclination angle of $i = 75.^\circ1$, over its kinematic centre (J2000) $17^{\rm h}49^{\rm m}26.^{\rm s}30$, $70^\circ08'40.''7$ (both determined by Greisen, Spekkens & van Moorsel 2009). The spatial distributions of the blue and red stellar samples corrected for projection are shown in Fig. 6 (bottom panel). It is interesting to note that the deprojected distribution of the blue young stellar population (Fig. 6 – bottom-left panel) is in remarkable agreement of the deprojected *GALEX* NUV data, presented by Freeland et al. (2010). Both distributions highlight the star-forming ring of the galaxy and its nucleus LINER (low-ionization nuclear emission-line regions; Lira et al. 2007), shown as a UV-bright clump at the centre of the ring (Freeland et al. 2010, their fig. 5). In the following section, we further compare the distribution of our blue stellar sample with that of the red sample, through their stellar surface density maps.

[6] It is interesting to note that the 4.5 μm image shows only a faint signature of a bar.

2.3 Stellar surface density maps

We construct stellar surface density maps for the blue and red samples with the application of the kernel density estimation (KDE), by convolving the stellar catalogues with a Gaussian kernel. The full width at half-maximum (FWHM) of this kernel specifies the 'resolution' at which stellar structures will be revealed. These density maps can be treated as significance maps, corresponding to two-dimensional probability functions for the positions of the stars in each sample. For their construction with this method, the most important (and debatable) parameter is the size of the KDE kernel (the convolving FWHM), i.e. the resolution of the constructed maps. At the distance of NGC 6503 (∼5.3 Mpc; Karachentsev et al. 2003), 1 arcsec corresponds to ∼25.7 pc, and therefore every WFC3 UVIS pixel (≃0.04 arcsec) corresponds to a physical scale of ∼1 pc. Consequently, a KDE map constructed from our data with a resolution of ∼10 pc requires a kernel with FWHM of ∼10 pixels (∼0.4 arcsec). However, such a map would be extremely noisy, revealing small compact stellar overdensities rather than coherent physically related stellar concentrations. The KDE kernel size to be applied depends on the science to be achieved from the KDE maps, and it is best decided based on experimentation. Our tests on various kernel sizes showed that an FWHM of ∼80 pc, comparable to the scale of typical OB associations (Gouliermis 2011, and references therein) and giant molecular clouds (GMCs; Bolatto et al. 2008, and references therein), is the most appropriate for the detection of large star-forming structures.

The stellar surface density maps of NGC 6503, constructed from our photometry with a kernel of ∼80 pc (80 UVIS pixels), for both the blue and red stellar samples are shown in Fig. 7. From the KDE map of the blue sample (Fig. 7 – left-hand panel), it is seen that the young blue stellar population depicts the inner star-forming ring of NGC 6503 (e.g. Mazzuca et al. 2008; Freeland et al. 2010), where individual large structures can be identified. On the other hand, the red stellar sample found in filters *F*555*W* and *F*814*W* is much more spread out, populating the whole extent of the disc of the galaxy. In the following sections, we further explore the clustering behaviour of young stars in NGC 6503. Specifically, we (a) conduct a census of young stellar structures, and determine their demographics, across the extent of the observed field of view, and (b) investigate the global distribution of the young populations and assess its hierarchy in order to understand the global star formation topology in NGC 6503.

3 YOUNG STELLAR STRUCTURES IN NGC 6503

The blue stellar population selected in the previous sections for the study of clustered star formation comprises 12 834 stars. Distinct concentrations of these young stars can be identified as stellar overdensities in the KDE stellar surface density maps. These overdensities correspond to individual star-forming structures, such as stellar associations, stellar aggregates and stellar complexes, the

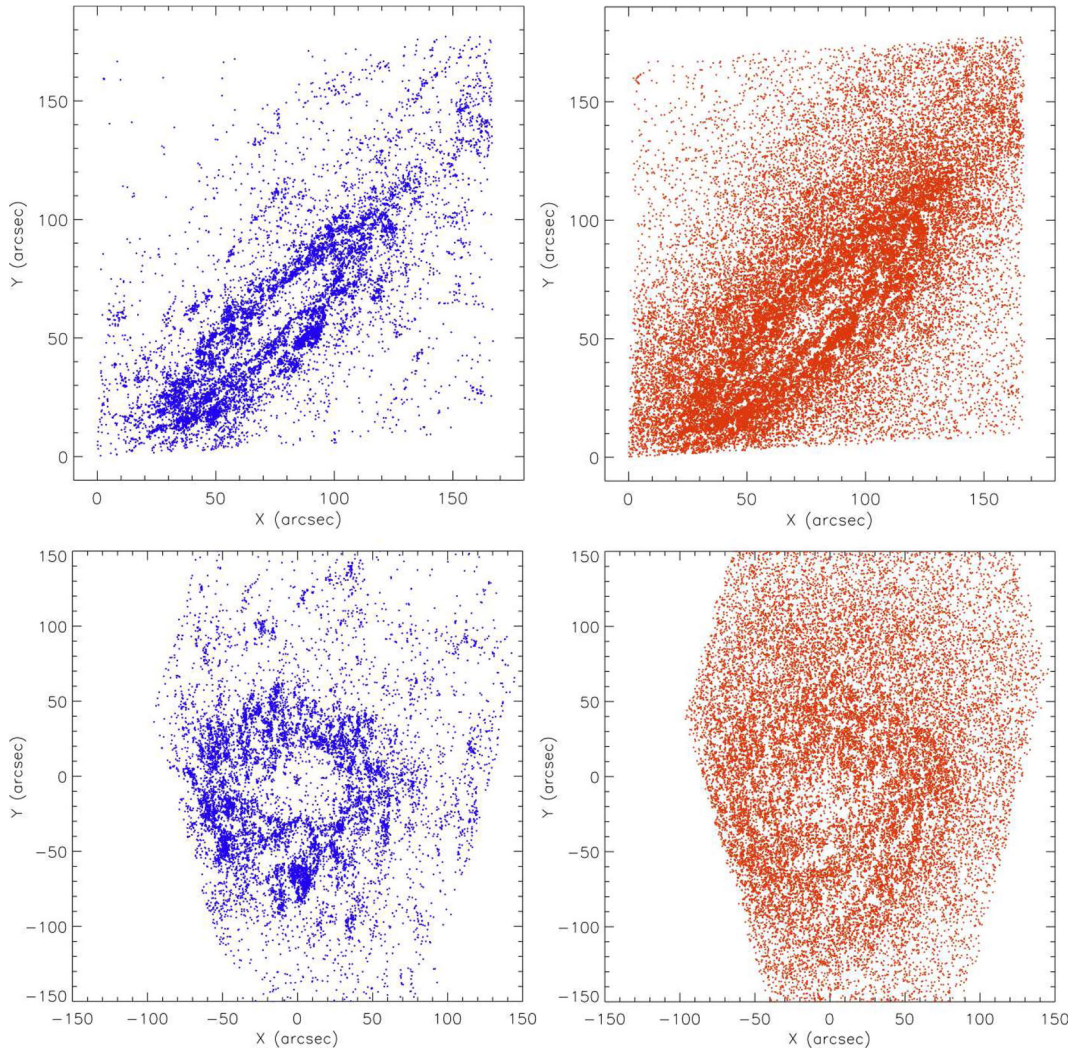

Figure 6. Top panels: spatial distribution of stars detected in two filter pairs with the best photometry. Left-hand panel: stars in the sample detected in the *F*275*W* and *F*336*W* filters ('blue' sample). Right-hand panel: stars detected in the filter pair *F*555*W* and *F*814*W* ('red' sample). Bottom panels: the same distributions deprojected for the inclination of the galaxy (see Section 2.2). The distribution of 'red' sources is more extended than the 'blue' sources, consistent with the prolonged dynamical mixing of these sources. The overall distribution of the red sources, however, still tracks partly star-forming regions of the galaxy. Gaps in the populated central areas of the red stellar distribution, and the lack of evidence of a central bar, are partially assigned to photometric incompleteness, while the lack of blue stars represents a true deficiency at the galaxy centre (see Section 4.1).

large-scale centres of star formation in a galaxy. The identification and characterization of these systems is thus important to our understanding of how galaxies construct their stellar components and what is their future evolution. In this section, we compile a detailed catalogue of all young stellar concentrations that can be revealed from our observations of NGC 6503. Our method is applied by first constructing the stellar surface density KDE map of Fig. 7, and then by identifying young stellar structures as stellar overdensities at specific significance levels, measured in σ above the average density, σ being the standard deviation of the background density (see e.g. Gouliermis et al. 2000, 2010, for more details on the method).

Independent repetitions of the detection method for different density thresholds, i.e. different significance levels, reveal young stellar concentrations across the complete dynamic range in stellar density. This process reveals smaller, denser stellar concentrations systematically belonging to larger and looser ones, providing the first evidence of hierarchical structural morphology in the distribution of the blue stars in NGC 6503. We refer to all these concentrations generally as *stellar structures*. In order to eliminate projection effects in our detection and the determination of the morphological parameters of the detected structures, we apply our method on projection corrected maps, such as those shown in Fig. 7.

3.1 Detected young stellar structures

Young stellar structures are identified on the KDE stellar surface density map of the blue stars. With 80 pc resolution we are able to identify loose stellar concentrations that correspond to the stellar associations and stellar complexes of the galaxy, while avoiding a high noise level produced by random small-scale density fluctuations. An isodensity contour plot of this surface density map is shown in Fig. 8 (left-hand panel). In this plot, contour lines correspond to different density levels, starting from that corresponding to the average density (0σ) up to the highest level of 16σ. They are drawn in steps of 1σ with different colours accordingly. These

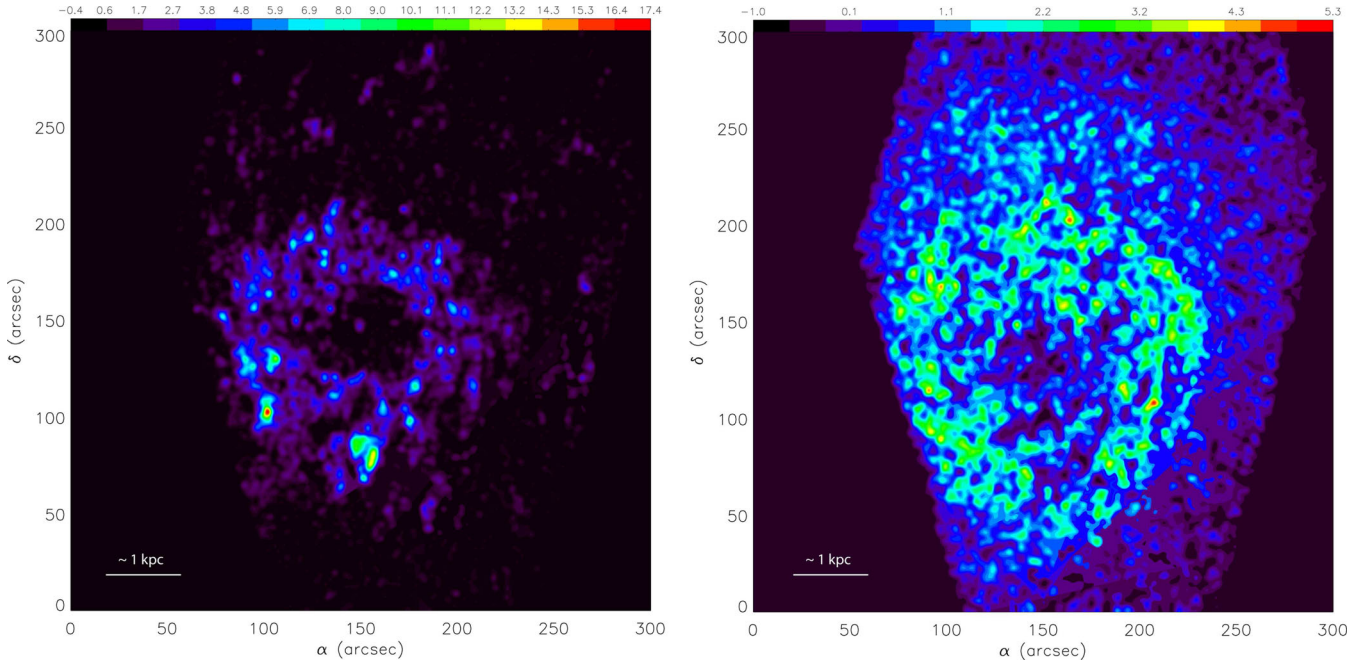

Figure 7. Surface stellar density maps constructed with the KDE method with a kernel of FWHM ∼ 80 pc, for stars identified with the best photometry in the filter pairs *F*275*W*, *F*336*W* (left-hand panel) and *F*555*W*, *F*814*W* (right-hand panel). The colour bar at the top corresponds to stellar density significance levels in values of σ, where σ is the density standard deviation in the whole of each sample. The 'blue' stellar population surface density tracks very well the star-forming ring of NGC 6503 (e.g. Mazzuca et al. 2008; Freeland et al. 2010). LEGUS photometry reveals individual star-forming structures across the ring in order to access the large-scale progression of star formation in space and time. On the other hand, the 'red' evolved stellar population is far more extensively distributed than the blue, populating the whole disc of the galaxy. This difference is consistent with the more prolonged dynamical mixing of more evolved populations, and their dissolution in the field of NGC 6503.

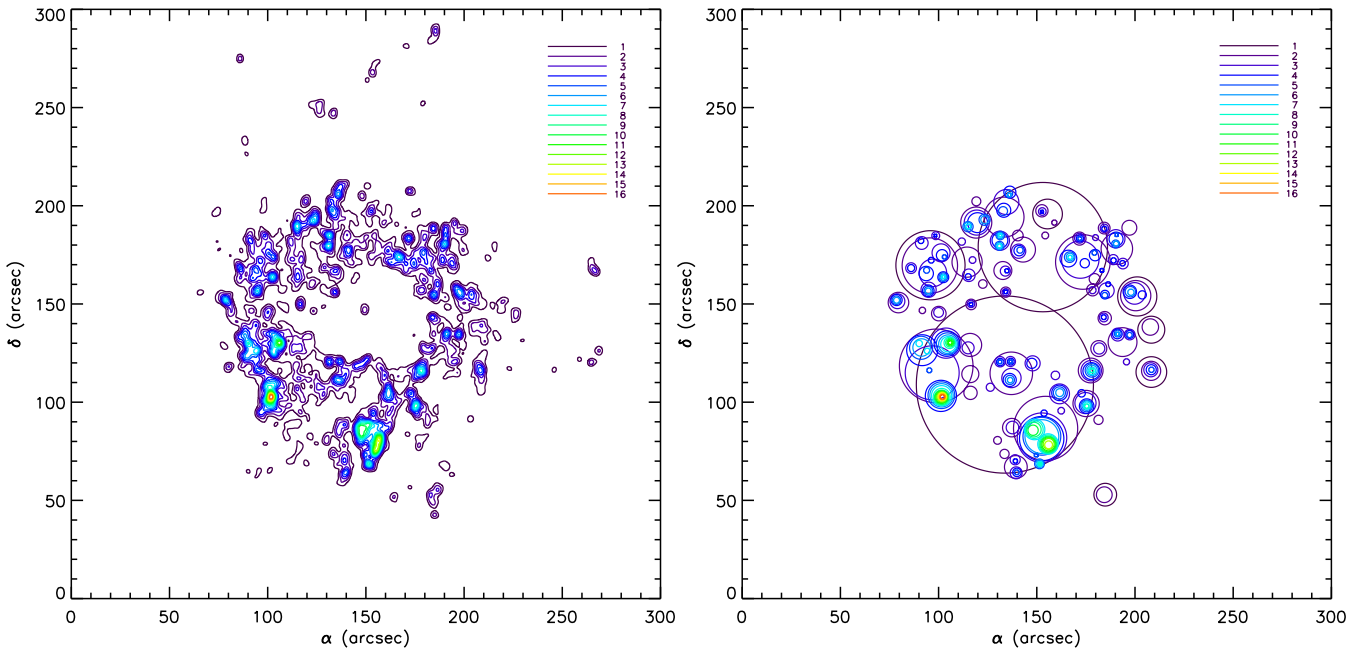

Figure 8. Left-hand panel: isodensity contour plot of the surface stellar density map constructed with the KDE method with a kernel of FWHM ∼80 pc, for the blue stars identified in both filters *F*275*W* and *F*336*W*. Right-hand panel: chart of the identified stellar structures, i.e. those which meet the criteria of including ≥5 stellar members, and appearing in at least two surface density significance levels. System borders are drawn with circles representing their sizes, $r_{\rm eff}$, as determined at the various significance levels, where they appear. In both panels, different colours are used for the isopleths and apertures of systems found at different significance levels in steps of 1σ.

Table 2. Survey of the young stellar structures in NGC 6503. Explanations on the characteristic parameters of the structures are given in the text (Section 3.1). Only the first 15 records of the survey are shown here for reference. The complete catalogue of 244 structures is available online at LEGUS site https://legus.stsci.edu/.

ID	σ	RA J2000 (deg)	Dec. J2000 (deg)	$N_\star$	Radius (pc) $r_{\rm eff}$	Radius (pc) $r_{\rm max}$	ξ	ρ ($\times 10^{-3}$) (stars pc^{-2})	$275_{\rm tot}$ (mag)	$336_{\rm tot}$ (mag)	$438_{\rm tot}$ (mag)	Family id.	Group id.
1	1	267.366 870	70.139 878	4388	1158.7	2424.7	2.093	1.04	13.73	14.21	15.13	1	1
2	1	267.360 523	70.146 816	2189	846.0	1572.5	1.859	0.97	14.68	15.13	16.02	2	21
3	1	267.399 790	70.138 429	643	452.4	670.2	1.481	1.00	16.26	16.67	17.57	3	36
4	1	267.324 116	70.151 839	206	255.9	353.4	1.381	1.01	17.12	17.30	17.93	4	37
5	1	267.315 085	70.150 455	114	200.6	375.2	1.871	0.91	18.18	18.55	19.43	5	38
6	1	267.360 586	70.148 180	97	194.2	252.0	1.298	0.83	18.26	18.74	19.43	6	39
7	1	267.317 336	70.151 773	77	176.4	238.8	1.354	0.80	18.92	19.26	20.13	7	40
8	1	267.325 148	70.143 415	62	148.4	212.8	1.434	0.91	18.58	19.02	19.78	8	41
9	2	267.392 443	70.135 681	1197	481.5	840.8	1.746	1.64	14.94	15.44	16.46	1	1
10	2	267.349 994	70.141 340	1007	419.9	1022.3	2.435	1.82	15.09	15.62	16.57	1	2
11	2	267.399 997	70.138 375	529	362.4	547.9	1.512	1.28	16.49	16.90	17.78	3	36
12	2	267.345 413	70.149 136	515	357.1	751.0	2.103	1.29	16.23	16.71	17.54	2	21
13	2	267.365 176	70.140 677	319	278.0	551.5	1.984	1.32	16.57	17.05	17.87	1	3
14	2	267.376 002	70.145 055	319	261.3	604.3	2.313	1.49	16.78	17.28	18.19	2	22
15	2	267.333 935	70.151 913	181	205.8	391.5	1.902	1.37	17.49	17.84	18.78	2	23

isopleths[7] determine the borders of various stellar structures identified across NGC 6503 at various significance levels. The physical dimensions of each detected structure are defined by these borders. A parameter considered in our detection is the minimum number of stars included in an overdensity in order to be classified as a structure, which is $N_{\rm min} = 5$, in line with other identification techniques (e.g. Bastian et al. 2007). This criterion eliminates the detection of random stellar congregations, so-called asterisms. Additionally, we consider as real those structures which appear in at least two significance levels, while we treat features that appear in only one (essentially the lowest 1σ) level as spurious detections. This criterion provides confidence that the identified overdensity is indeed a physical stellar concentration.

The catalogue of identified stellar structures in NGC 6503 consists of 244 systems, revealed at significance levels between 1σ and 16σ. In Table 2, we show a sample of the first 15 records of this catalogue and their measured parameters. The complete catalogue of all identified young stellar structures is available online. In columns 1 and 2, the ID number and the detection density threshold (in σ) are given for every object. Columns 3 and 4 provide the celestial coordinates of the structures' barycentres, which correspond to their KDE density centres. Column 5 shows the number of the blue stars included within the borders of every structure, as defined by the corresponding isopleth. A measure of the size of each system is the so-called *effective radius* (e.g. Carpenter 2000) or *equivalent radius* (e.g. Román-Zúñiga et al. 2008), defined as the radius of a circle with the same area as the area covered by the system. We provide two measurements for this radius: (1) the radius determined by the area $A_{\rm CH}$ enclosed by the convex hull of the system ($r_{\rm eff} \equiv \sqrt{A_{\rm CH}/\pi}$, column 6) and (2) the radius defined by the area $A_{\rm max}$ enclosed by the largest circle that encompasses the entire system ($r_{\rm max} \equiv \sqrt{A_{\rm max}/\pi}$, column 7), equivalent to the half of the distance between the two furthest sources in the system.

The ratio of these two radii provides a characterization of the *elongation* of each system $\xi \equiv r_{\rm max}/r_{\rm eff}$, which we provide in column 8. Schmeja & Klessen (2006) showed that the estimation of the system's area from its convex hull makes ξ a reliable measure for the elongation, since it excludes the possibility that fractal substructure in an otherwise spherical structure can lead to unrealistic elongations. These authors also determined the increase of ξ with increasing axial ratios of elliptical distributions. A circular distribution (axial ratio = 1) has $\xi \simeq 1$. From the number of blue stars enclosed within the borders of each structure (column 5) and its radius $r_{\rm eff}$ (column 6), we also have a measurement of the surface stellar density of each structure, which is given in column 9 of Table 2. These stellar structures contain blue stars in the whole observed magnitude range of $F336W \lesssim 26$. The total brightness of each system, calculated from its stellar population in the three blue filters (i.e. $F275W$, $F336W$ and $F438W$), is given in columns 10, 11 and 12, respectively.

A histogram of the numbers of all detected structures per detection density level up to 10σ is shown in Fig. 9. This distribution peaks at the detection levels of 2σ, 3σ and 4σ, which determine the vast majority of the detected structures. Higher detection levels mostly reveal the high-density peaks of the same structures, as well as their 'offspring' structures which they break into. A chart of the detected structures is shown in Fig. 8 (right-hand panel). In this map, the structures are indicated by circles equivalent to their measured sizes. Apertures with radii equal to $r_{\rm eff}$ of the detected systems are drawn in different colours according to the density threshold where the structures were detected (as in the isopleth plot at the left-hand panel of the figure).

As shown in Table 2, and can be seen in the maps of Fig. 8, there are eight large structures identified at the 1σ level. Two of them extend to the 2σ level, and appear isolated, i.e. not related to other large structures. Three additional 1σ structures appear also in few intermediate density levels ($\geq 2\sigma$), two of them also showing a second substructure. The remaining three 1σ structures are extended stellar concentrations that qualify as large *stellar supercomplexes* with dimensions between 1 and 2 kpc. These structures comprise the vast majority of identified stellar structures, which are themselves *multiple* concentrations seen at higher density levels. The 2σ concentrations most probably correspond to the so-called *stellar aggregates* and *stellar complexes* of the galaxy, while the structures detected at the 3σ level are actually members of these

[7] The noun 'isopleth' is used to define every line on the map that connects points having equal numeric value of surface stellar density; origin from the Greek *isoplēthēs*, equal in number.

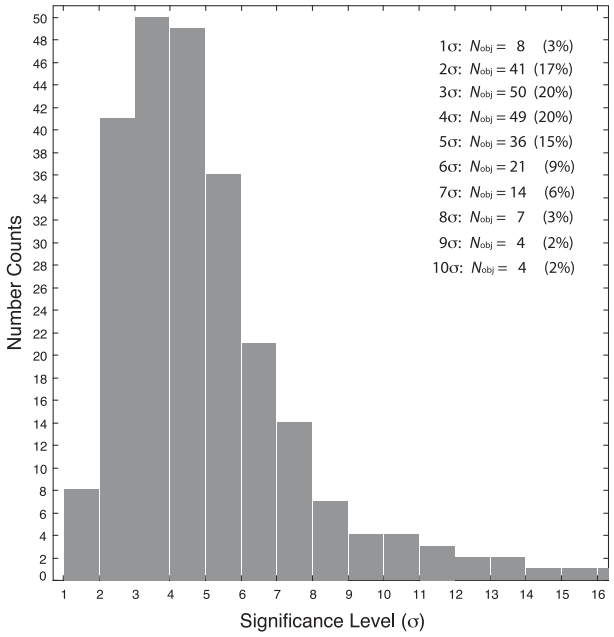

Figure 9. Histogram of the numbers of detected young stellar structures per significance level in NGC 6503. The majority of the structures are revealed at the 2σ, 3σ and 4σ levels. They represent the population of stellar aggregates and complexes of the galaxy. All detected structures are members of eight extended structures found at the 1σ level. Three of them are large super-structures encompassing 95 per cent of the total structure population.

concentrations, fulfilling the typical image of hierarchical structuring of stars on a galaxy scale. Even higher density detections ($\geq 4\sigma$) correspond to the more condensed stellar density peaks of the larger structures.

We define each of the structures revealed at the 1σ level as a *family* of structures. We also determine as members of a *group* structures that are 'spawned' from the same single structure. In total, we identify 82 groups divided into eight families, three of which are large super-complexes that encompass 95 per cent of all revealed stellar structures. The family and group numbers of each structure are given in columns 13 and 14 of Table 2, respectively.

3.2 Structure tree

In this section, we visualize the 'family ties' of high-density structures in relation to their parental super-structures. The 'breaking' of super-structures of specific low density level into several, smaller and denser substructures at higher density levels provides the first evidence of a morphological hierarchy in the way young stars are clustered across the ring. An intuitive way to illustrate hierarchical structures is through the so-called *dendrograms*, introduced as 'structure trees' for the analysis of molecular cloud structure by Houlahan & Scalo (1992), refined by Rosolowsky et al. (2008). A dendrogram is constructed by identifying in the stellar surface density map connected structures found at different density thresholds, while keeping track of the connection to 'parent structures' (on a lower level) and 'child structures' (on the next higher level, lying within the boundaries of its parent). In the dendrogram of a geometrically perfect hierarchy, each parent would branch out into the same number of children at each level.

We construct the dendrogram of the stellar structures detected in NGC 6503 at various density thresholds, up to the highest level of 16σ above the background density. In this dendrogram, shown in

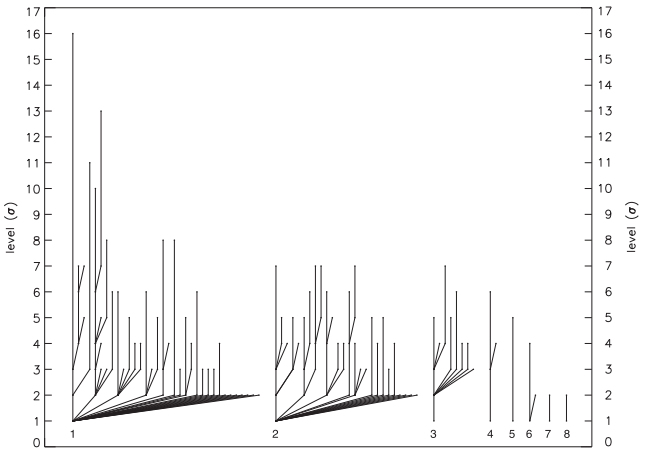

Figure 10. Dendrogram (structure tree) of the stellar structures identified at different significance levels in the KDE density map (Fig. 8), illustrating the hierarchy in the manner stellar structures of blue stars are assembled. This dendrogram also demonstrates the hierarchical behaviour in the global clustering of these stars across the whole galaxy, which we quantify in more detail in Section 4.2. Parental super-structures, identified at 1σ level, are indicated by their identification numbers.

Fig. 10, the structures found at each density level are represented not only by the 'leaves' that end at the particular level, but by all branches present at that level. For example, at the 3σ level, there are 50 branches of the dendrogram (regardless whether they end at this level, continue to a higher level as a single system, or split into two or more branches), corresponding to the 50 detected stellar structures. This dendrogram demonstrates that most structures split up into several substructures over few levels. The combination of this dendrogram with the maps of Fig. 8 illustrates graphically the hierarchical spatial distribution of young stars in NGC 6503.

3.3 Parameter demographics

Our survey of young stellar structures (Table 2) covers a variety of systems, starting with those including the minimum of six to eight stellar members with dimensions $\lesssim$40 pc (e.g. structures 148 and 226), up to those with maximum size of more than 1 kpc, including over 1000 stars (i.e. structure 9). The parameter demographics of the stellar structures, revealed at various significance levels, are given in Table 3. These parameters include the average size (column 2), size dispersion (column 3), the average elongation (column 4) and the average surface stellar density (column 5) of all structures found in each density level. The total numbers of stars and total UV magnitudes of all structures in each level are also given (columns 6 and 8, respectively). Table 3 provides the fraction of stars at each significance level relative to the total young stellar sample (column 7), and the corresponding stellar UV flux fraction relative to the total observed UV flux per detection level (column 9).

In general, almost all parameters given in Table 3 show a dependence on the detection level.[8] The average size (and its dispersion) decreases with increasing density level, with a plateau and a small bump towards relatively larger sizes for levels between 6σ and 12σ. The mean and median of the sizes reported in column 2 of Table 3 are equal to 185 pc and 138 pc, respectively. Both the total stellar number and total UV brightness show a systematic correlation

[8] Among all parameters, only elongation, ξ, seems to be independent of the level of detection for the structures.

Table 3. Demographics of the young stellar structures revealed in the KDE surface stellar density map at various significance levels. In column 1, the detection levels (in σ) are given. The parameters shown are the average size (column 2), size dispersion (column 3), the average elongation (column 4) and the average surface stellar density (column 5) of the structures in each density level. The corresponding total stellar numbers ($N_\star$, column 6) and UV magnitudes (m_{275}, column 8) per density level are also given, along with the corresponding fractions of these parameters over the total observed number of stars, $N_{\star,\,\rm tot}$, and total observed stellar UV flux, $m_{275,\,\rm tot}$, shown in columns 7 and 9, respectively. There are no dispersions given for the parameters in the last three entrances, because there is only one object found in each of the corresponding density levels.

Detection level (σ)	Size S (pc) $\bar{S}$	σ_S	$\bar{\xi}$	$\bar{\rho}$ ($\times10^{-3}$) (stars pc^{-2})	$N_\star$	$f_\star$ $N_\star/N_{\star,\,\rm tot}$	m_{275} (mag)	$f_{\rm UV}$ $m_{275}/m_{275,\,\rm tot}$
(1)	(2)	(3)	(4)	(5)	(6)	(7)	(8)	(9)
1	858	751	1.60 ± 0.30	0.93 ± 0.08	7776	0.606	13.2	0.699
2	295	210	1.49 ± 0.39	1.46 ± 0.20	6126	0.477	13.3	0.603
3	202	132	1.32 ± 0.29	1.97 ± 0.26	4371	0.341	13.6	0.474
4	148	104	1.30 ± 0.33	2.94 ± 1.00	3070	0.239	13.9	0.367
5	127	94	1.17 ± 0.20	3.46 ± 0.84	2043	0.159	14.2	0.283
6	129	97	1.22 ± 0.28	3.86 ± 1.04	1400	0.109	14.5	0.211
7	121	88	1.18 ± 0.26	4.80 ± 1.54	907	0.071	14.8	0.151
8	142	92	1.21 ± 0.29	5.20 ± 2.11	623	0.049	15.1	0.117
9	179	45	1.34 ± 0.19	4.55 ± 0.52	475	0.037	15.3	0.099
10	146	47	1.31 ± 0.23	5.15 ± 0.90	362	0.028	15.5	0.082
11	125	63	1.32 ± 0.39	6.08 ± 0.80	243	0.019	15.8	0.063
12	138	6	1.47 ± 0.48	6.05 ± 0.60	179	0.014	16.0	0.052
13	110	10	1.57 ± 0.56	6.43 ± 0.56	121	0.009	16.2	0.044
14	99	–	1.14	7.50	57	0.004	16.8	0.024
15	81	–	1.24	8.99	45	0.004	17.0	0.021
16	59	–	1.07	6.87	18	0.001	17.4	0.014

with the detection significance level, with larger and sparser stellar structures hosting higher stellar numbers and UV brightness. This agreement in the trends of these two parameters can be directly explained by the almost one-to-one correlation between their values, as can be derived from the data of Table 3.

A systematic dependence on level also exists for the fraction $f_\star$ of stars included in every density level over the total observed number of blue stars. This fraction changes from 60 per cent within the 1σ structures to $\sim$1‰ at the highest density level (corresponding to one structure identified at the 16σ level). However, while the same dependence on significance level is found for the fraction of UV emission per level relative to that observed from all blue stars (column 9 in Table 3), this trend is steeper than that for stellar fraction. In particular, while $\sim$60 per cent of the stars (i.e. the 1σ structures) produce $\sim$70 per cent of UV, this correlation changes for structures with higher densities. For example, at 7σ significance, where $\sim$7 per cent of the total young population resides, $\sim$15 per cent of the total UV brightness is produced. At even higher levels, only a few ‰ of the total young stellar population in NGC 6503 emits few per cent of the total UV light (see Table 3). This comparison suggests that compact structures, identified at higher density levels, encompass on average the UV-brightest stars in the galaxy. This result is elaborated more in Section 4.3, where we discuss the clustering behaviour of blue stars as a function of their brightness.

The size distribution of all detected structures constructed by binning them according to the logarithm of their dimensions is shown in Fig. 11. Dimensions are given in physical units (pc), and they are derived from the effective radii of the structures. A functional fit of this histogram to a normal distribution, drawn with a red line, shows that the dimensions of the detected systems are clustered around an average of $\simeq$ 120 pc with a standard deviation of $\simeq$ 40 pc. This is an interesting result, considering that this size is comparable (but still to the upper limit) to the typical size for GMCs (e.g. Cox 2000; Tielens 2005). It has been also pointed out earlier by various authors (e.g. Efremov, Ivanov & Nikolov 1987; Ivanov 1996) that young stellar associations in different galaxies have dimensions that average at $\sim$80 pc, comparable to the 40 per cent of our distribution. Considering that the determination of structures dimensions is sensitive to the resolution of their detection, the question if this length-scale would represent a characteristic scale for star formation

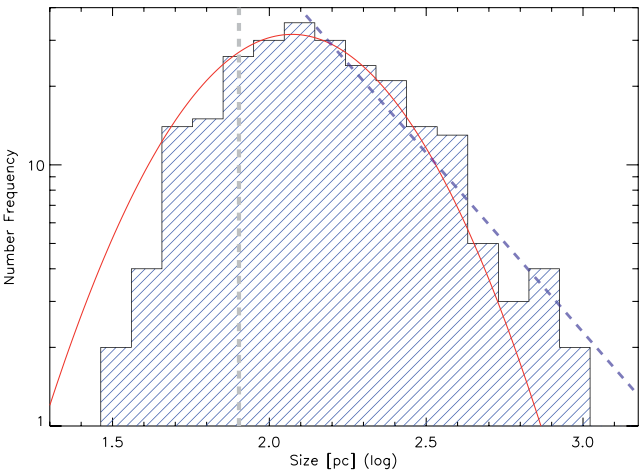

Figure 11. Histogram of the size distribution of all detected young stellar structures in NGC 6503, with a logarithmic bin size of 0.075. Sizes are defined as $2 \times r_{\rm eff}$ and are given in pc. The distribution peaks at a size of $\sim$130 pc. The best-fitting Gaussian (red line) peaks at an average size of $\sim$120 pc, close to the smoothing radius used for the structure identification of 80 pc (indicated with the vertical grey dashed line). This fit shows that the right-hand part of the size distribution, corresponding to the resolved structures, behaves almost like a power law (indicated by the blue dashed line).

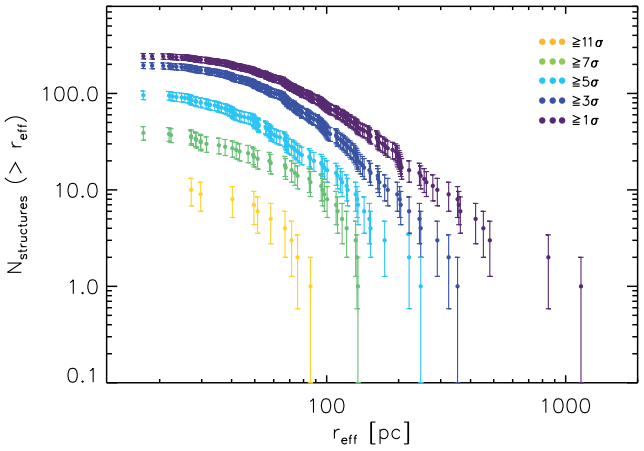

Figure 12. Radius cumulative distribution functions derived from the NGC 6503 survey of star-forming structures. The results for five different detection density levels are shown. The distribution of structures found at levels $\geq 1\sigma$ (purple symbols) corresponds to the total sample. This distribution and those for samples including low-density structures (blue symbols) show power-law tails at large radii. The distributions for samples constrained to high-density structures (green and yellow symbols) have shapes closer to lognormal.

is still open (e.g. Bastian et al. 2007; Gouliermis 2011). Moreover, the detection resolution seems to also determine the peak of this distribution. By repeating the analysis after smoothing by smaller scales (between 70 and 40 pc), we found that indeed the peak moves at smaller values (from ∼120 pc at 80 pc resolution to ∼70 pc at 40 pc resolution).

From this fit it is seen that the size distribution of our structures is not lognormal. There is a deficiency in the number of small-scale structures at the left-hand tail of the distribution, which falls below the Gaussian. This deficiency is most probably due to incompleteness introduced by the smoothing, since it seems to be more important for the distributions derived with larger smoothing kernels. In addition, the right-hand part of the distribution, for structures with sizes larger than ∼120 pc, is more extended than the Gaussian and has a power-law shape. This is demonstrated with a power-law fit, shown with the blue dashed line, which indicates a scale-free behaviour. It is interesting to note that the power-law behaviour of the right part of the distribution seems to be independent of the smoothing kernel, having almost the same exponent of ~ -1.5 for distributions produced after smoothing with smaller kernels.

This power-law behaviour is further supported by the cumulative radius distribution of the star-forming structures found in different density thresholds (levels), shown in Fig. 12. The distributions of structures found only within five indicative detection significance levels are shown to avoid confusion. The cumulative distribution functions of radii for all structures or those including low-density structures (purple and blue symbols in Fig. 12) do not have lognormal shapes, at least in their entirety, with clear power-law tails at large radii. On the other hand, the distributions for detections at higher density thresholds (e.g. green and yellow symbols in Fig. 12) demonstrate a behaviour closer to lognormal.

3.4 Parameter correlations

The correlation of physical parameters of star-forming structures provides insight into the processes and conditions that dictate their formation and evolution. If these systems do trace gas structure, then their fundamental properties should be tightly related to those of GMCs, and should have comparable correlations, which nevertheless should also be affected by the galactic dynamics and the transformation of gas to stars. In this section, we explore the correlation of the structural parameters measured for the discovered stellar structures in order to identify the factors that determined those relations. The basic parameters considered are those directly measured from our data, namely the size of the structures (determined as two times their $r_{\rm eff}$), their surface stellar density, μ (in stars pc^{-2}), the number of member stars, $N_\star$, and their total UV brightness, m_{275}, in magnitudes.

We also make a rough estimate of the volume stellar density of each structure, ρ (in stars pc^{-3}), assuming spherical symmetry, as $\rho \propto \mu\, r_{\rm eff}^{-1}$. This estimation for elongated structures, which are typically the larger low-density structures, is expected to suffer from the lack of symmetry. However, we determine the volume density within the effective radius and not the maximum radius, which defines the largest aperture covered by the structure, and includes a large fraction of empty areas. Thus, we eliminate to a large extent the bias in the volume density estimation due to asymmetries.

3.4.1 *Stellar number correlation with radius*

To measure molecular cloud structure, Kauffmann et al. (2010a,b) established the correlation between mass and radius for clouds in the solar neighbourhood. Using the survey of stellar complexes of the present work, we can test such a relation for large star-forming structures. As a first-order approximation, the number of stars in a group is directly proportional to its mass, assuming that all groups are of similar age and as long as sampling effects of the mass function are not significant. In Fig. 13, we show the measured radii, $r_{\rm eff}$, versus the number of stars within each identified structure. The solid line in the plot represents the least-squares linear fit to the logarithms of the data. While there is no significant scatter

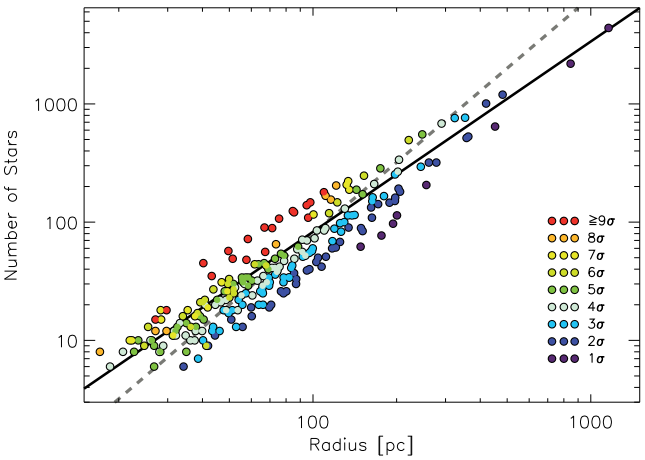

Figure 13. Correlation of number of stars with the radius, $r_{\rm eff}$, of the detected stellar structures. The different coloured points represent structures identified at different density levels, indicated by the legend. The black solid line is the best fit through all the data, with a slope of 1.6. This fit for the various significance structures varies in agreement with previous investigations. This power-law behaviour is expected from a fractal stellar distribution. A slope of 2, corresponding to constant stellar surface density, is shown with the grey dashed line to indicate how a uniform distribution appears in this correlation.

in the whole sample, the relation for systems identified at lower density thresholds is different from that for those found at higher densities with indices varying between about 1.5 and 2. This trend is consistent with that found by Gouliermis et al. (2003) for 494 stellar associations and open clusters in the Large Magellanic Cloud.

A single power-law mass–size relation with a fractional index is expected from a fractal distribution of young stars (in agreement with, e.g. Elmegreen & Falgarone 1996). A uniform two-dimensional distribution of stars would correspond to a constant surface stellar density, and therefore the number of stars (or mass) would be proportional to the radius (or size) as $\propto \pi r^2$. Thus, a uniform stellar distribution would also produce a power-law behaviour but with an index 2 due to the dependence of surface on radius. This relation is shown with a dashed line in Fig. 13. Concerning structures in our sample, the correlation between number of stars and radius for the low-density structures (up to 3σ) has slopes very close to 2, indicating that these systems have constant surface densities. On the other hand, the high-density systems show correlations different from a uniform distribution with slopes between 1.5 and 1.8 (all slopes have about 1 per cent uncertainty), consistent with self-similar stellar distributions. Such a dependence of the mass–radius relation to the detection threshold is also found in M33 by Bastian et al. (2007, who used a different technique), summarizing the differences in the trends of properties for different types of stellar systems. We explore these differences in the following section.

3.4.2 *Surface and volume stellar density correlations with size*

Correlations between the surface stellar density μ and volume stellar density ρ of the young stellar structures to their sizes L (in pc) are shown in Fig. 14. Points are coloured according to the detection surface density level (in σ) of the corresponding structures. Both plots show an overall dependence of stellar density on size, with that for the volume density being more prominent. However, if structures are grouped according to their density detection levels, at the top panel of Fig. 14 it can be seen that there is no clear dependence of surface density on size for low-density structures, in particular those identified at levels $<5\sigma$, showing almost flat distributions of points. This is not the case for the high-density (more compact and smaller) structures.

The volume density–size correlation, shown in the bottom panel of Fig. 14, can be represented for all points by a power law of the form $\rho \propto L^{-\alpha}$, with index $\alpha = -1.33$, established with a linear fit to the data (grey thick line in the plot). However, as can be seen in the plot, this slope differs for structures identified at different density detection levels, with low-density (and larger sizes) structures following a more shallow relation than the high-density structures. We demonstrate the dependence of the exponent α for our stellar structures on their detection density level in Fig. 15, where we plot α, as found for every group of structures, as a function of the corresponding density threshold (in σ).

The correlation between volume densities and sizes we establish for the detected stellar structures can be directly compared to that determined by Larson (1981) for molecular clouds, and confirmed by other authors (e.g. Myers 1983; Solomon et al. 1987; Heyer et al. 2009).[9] The so-called Larson's third relation exhibits the tendency

[9] It should be noted, though, that while our structures for detection levels $\leq 6\sigma$ have sizes larger than ∼100 pc, most of the molecular clouds in the Milky Way have sizes of that order or less.

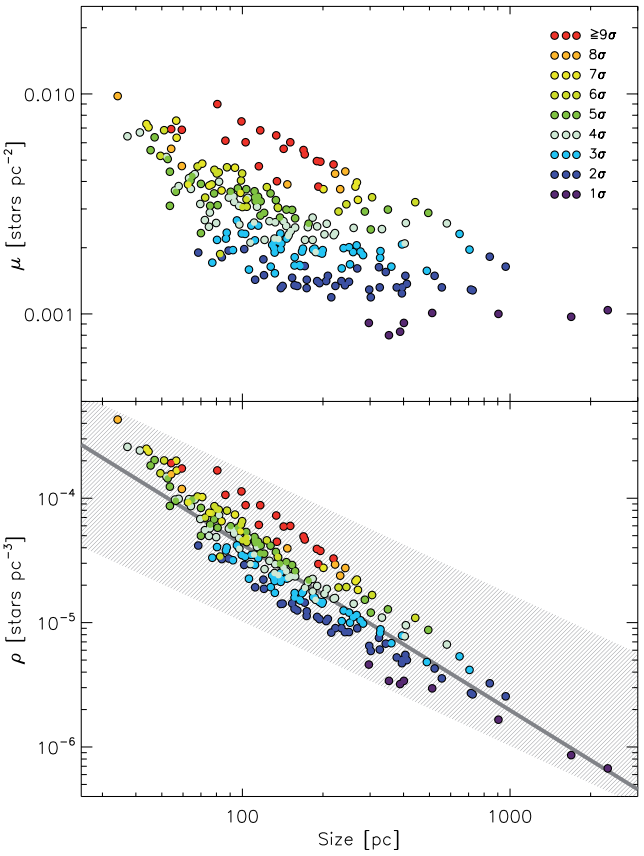

Figure 14. Surface stellar density (top) and volume stellar density (bottom) correlation with the size of the detected stellar structures. In the top panel, it is shown that the surface density of low-density (large) structures, in particular those detected at levels lower than $\sim 5\sigma$, is almost constant, in contrast to the high-density systems, where a correlation between surface density and size is more apparent. On the other hand, volume density, plotted in the bottom panel, shows a clear correlation with size for all structures, with different exponents for structures found at different density levels. The shaded area represents Larson's third relation, which correlates the sizes of molecular clouds to their volume densities. The correlation found for our stellar structures seems to comply with this relation, although it has a trend to be on average steeper (fit is shown with the thick line). The correlation for systems detected at levels lower than $\sim 5\sigma$ is more compatible to Larson's relation than those for systems found at levels $\gtrsim 5\sigma$, which are steeper (see also Fig. 15).

of the mean cloud volume density, ρ (in cm^{-3}), to scale inversely with the cloud size, $\rho \propto L^{-1.1}$. Larson's exponent of -1.1 is indicated by a horizontal dash–dotted line in Fig. 15. This exponent coincides with α determined in our correlation for structures at density levels between $\sim 5\sigma$ and 6σ.

Larson's relation implies that clouds have approximately constant column densities, i.e. the same significance levels relative to a fixed background, reflecting the identification of molecular clouds as constant-density objects (Solomon et al. 1987). In the case of our stellar structures, as seen in Fig. 14 (top panel) this does not apply, since the identification of these structures is made at various density levels. Only structures detected at low density levels ($<5\sigma$) have surface stellar densities almost independent of their size, and $\rho(L)$ relations comparable to Larson's relation (α values below the 1.1 limit in Fig. 15). In contrast, high-density structures have steeper $\rho(L)$ relations, because their $\mu(L)$ relations are not flat. These steeper correlations are the result of the higher densities of structures that

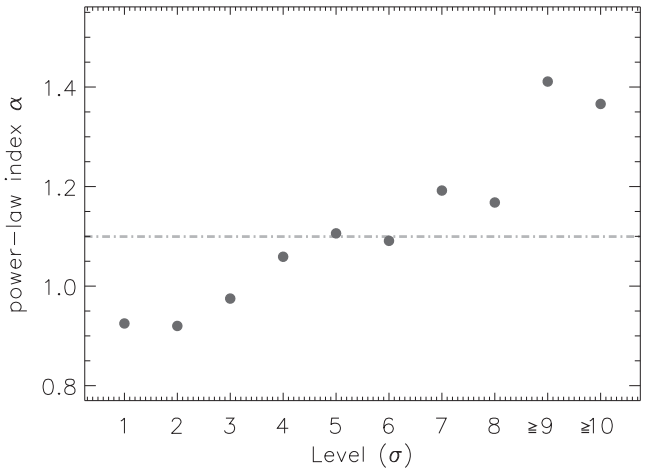

Figure 15. Relation between the index α in the relation $\rho \propto L^{-\alpha}$ for the detected stellar structures and the corresponding detection density level (in σ). This plot shows a dependence of the correlation between volume stellar density and size of the structures to their detection limits. The size of large, low-density structures (found at levels up to $\sim 5\sigma$) seems be correlated to their corresponding volume density in a fashion comparable to or flatter than Larson's third relation (indicated by the horizontal dash–dotted line), while high-density, smaller structures have clearly steeper correlation between their sizes and volume densities.

tend to be smaller, and reflect the steeper density profiles of these systems (as $\propto r^{-\alpha}$ for spherical systems) in relation to those of low density.

4 THE GLOBAL CLUSTERING OF YOUNG STARS IN NGC 6503

4.1 Stellar surface density profiles

We construct the radial stellar surface density profile across the observed field of view of the blue stellar population of NGC 6503, by counting the stars in concentric annuli around the rotational centre of the galaxy (defined in Section 2.2). The annuli are determined in logarithmically increasing radial distances, so that the width of each annulus increases with its radial distance. The cumulative radial stellar surface density profile of the blue stellar population of NGC 6503 is shown in Fig. 16 (top panel). In this figure, the profile of the red population, as this stellar sample is determined in Section 2.1, is also shown for comparison (bottom panel).

From these profiles, it is seen that blue and red stars follow quite different radial distributions around the centre of the galaxy. Specifically, the blue stars show a very strong peak at the centre, where the LINER is located. The surface density drops rapidly within a very short radial distance ($\sim$14 arcsec $\sim$0.35 kpc) and then rises sharply, reaching a peak at a distance of $\sim$1.9 kpc (Fig. 16, top). The distribution of the red stars also shows central densities lower than those at larger radii, but their deficiency in the inner part of the galaxy is not as severe as for the blue stars. Nevertheless, the surface density of red stars rises slowly outwards and peaks at a distance of $\sim$2.1 kpc, a distance comparable to that where the blue stellar distribution peaks. It drops again at larger distances, but far more slowly than that for the blue stars (Fig. 16).

We evaluated the deficiency of stars in the galaxy centre in terms of incompleteness in our photometry due to crowding. Our artificial star experiments showed that the lack of blue stars in the circumnuclear region is not due to photometric incompleteness. The number of UV sources is apparently very small and thus the blue stellar sample is flux-limited rather than crowded-limited even at the centre of NGC 6503. The situation is different in the optical filters, as for example in the *F*555*W* filter, which is found to be clearly more incomplete in the centre than in the periphery. As a consequence, the circumnuclear decreases seen in the stellar profiles of Fig. 16 are probably due to different reasons. While the central lack of blue sources is due to the real absence of a significant (and dense) young population in the centre, the central deficiency of red stars is due (at least in part) to incompleteness.

Both surface density profiles shown in Fig. 16, and in particular that of the blue young population, track the inner star-forming ring of

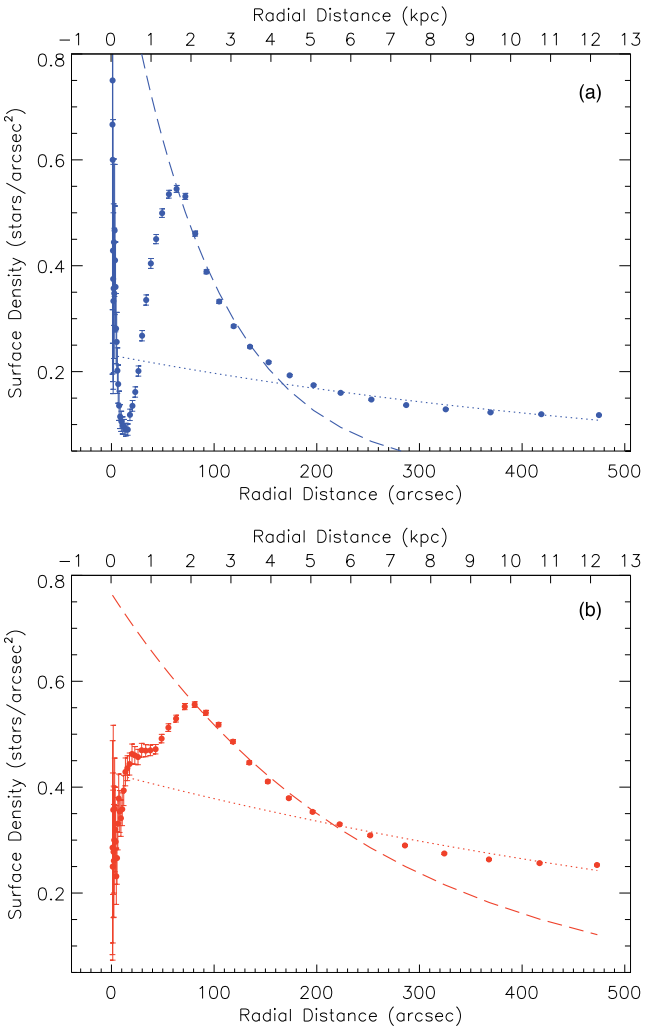

Figure 16. (a) Cumulative radial stellar density profile of the blue stellar population in NGC 6503. This profile exhibits the ring-shaped distribution of the youngest populations, highlighting the very low abundance of young stars in the inner parts of the galaxy. In this profile, the star-forming ring peaks at a radial distance $\sim$72 arcsec$^{+10}_{-8}$, corresponding to $\sim 1.85^{+0.26}_{-0.21}$ kpc. (b) The corresponding profile of the red population shows a different behaviour, with a much lower deficiency of stars in the inner parts, and a peak at somewhat larger radial distance of $\sim$81 arcsec$^{+11}_{-10}$ ($\sim 2.09^{+0.28}_{-0.26}$ kpc). Exponential disc fits of the profiles are shown with dashed lines. These fits, equivalent to those on the surface brightness profiles previously presented (Bottema 1989; Freeland et al. 2010), do not fit the outskirts of the observed distributions, which are fitted with different exponential profiles (shown with dotted lines).

the galaxy with a peak at ∼2 kpc. This is in line with the previously published radial luminosity profile of NGC 6503, which is proposed by Bottema (1989) as a typical example of Type II (Freeman 1970), i.e. of the form $I(R) < I_0 e^{-\alpha R}$ for a radial distance interval not far from its centre. At larger radial distances, both our blue and red profiles drop in an exponential fashion, as shown by the fitted exponential disc models plotted with dashed lines on the observed profiles of Fig. 16. These exponential disc models agree with those describing the smooth surface brightness profile of the galaxy in various wavelengths for radial distances up to about 3 kpc (Freeland et al. 2010). However, in order to describe the distribution of stars at the outskirts of our stellar surface density profiles for radial distances $\gtrsim$4–5 kpc, fits to additional exponential discs were considered. These fits are plotted in the profiles of Fig. 16 with dotted lines.

A Type II profile produced by a stellar deficit in the inner parts of the galaxy may be caused by (1) dust extinction, (2) an inner truncated disc or (3) a ring of bright stars. An exponential disc and a truncated light profile due to dust extinction are proposed for NGC 6503 by Bottema & Gerritsen (1997), but a statistical study on several galaxies showed that the possibility of dust extinction causing Type II profiles is inconclusive (MacArthur, Courteau & Holtzman 2003). Concerning the other two possibilities, a truncated disc in NGC 6503 implies that there is a genuine mass deficit in the inner region of the galaxy, and a stellar ring relates to bar formation. The dynamics of NGC 6503 was modelled by Puglielli, Widrow & Courteau (2010) with a Bayesian inference by assuming a Kormendy (1977) truncated disc. These authors found that the disc of NGC 6503 is indeed equally well fitted by either mechanisms, i.e. an inner truncated profile or a ring formation by a bar.

The inner drop of stellar density seen in our profiles also agrees with a sharp decrease in the velocity dispersion (σ-drop) for radii smaller than ∼10 arcsec (∼0.25 kpc) observed by Bottema (1989) with a minimum at a distance remarkably similar to that of our blue stellar surface density profile.[10] Modelling of the dynamics of the galaxy, however, could not provide a reliable theoretical description of the inner drop in dispersion (Bottema & Gerritsen 1997). In their study, Puglielli et al. (2010) found that the mass–luminosity ratio of NGC 6503 pseudobulge is lower than that in the disc, suggesting the presence of a dynamically-cold star-forming component that is probably responsible for the velocity dispersion drop, in agreement with previous studies (Wozniak et al. 2003; Comerón, Knapen & Beckman 2008). The existence of an inner nuclear bar could also produce the σ-drop, as has been reported in the literature for some cases (de Lorenzo-Cáceres et al. 2008). Indeed, while the ring of NGC 6503 is not considered to have the classical aspect of dynamically induced resonance rings (Mazzuca et al. 2008), it is likely an *inner ring and not a nuclear ring*, possibly caused by a strong end-on bar which is embedded inside it (Knapen et al. 2006; Freeland et al. 2010).

4.2 Hierarchical structure in stellar clustering

As discussed in Section 3, young stellar structures in NGC 6503 are assembled in a hierarchical fashion, in the sense that there are condensed structures belonging to larger looser ones, which themselves are part of even larger low-density stellar systems. This behaviour, demonstrated visually in the dendrogram of Fig. 10, suggests that the morphology of young stellar cluster assembling across the whole galaxy is self-similar. In this section, we quantify the young stellar clustering behaviour with the use of the two-point correlation function and we determine the time-scale within which stellar clustering sustains its behaviour.

The spatial distribution of stars can be quantified with the construction of the two-point correlation or autocorrelation function (ACF), which is a measure of the degree of clustering in the spatial distribution, $\xi(r)$, of a sample of sources (Baugh & Murdin 2000). This method, introduced by Peebles (1980) in cosmology, has been successfully used for characterizing the stellar clustering behaviour in star-forming regions in the Milky Way (e.g. Gomez et al. 1993; Larson 1995), as well as that of stellar populations and star clusters in remote galaxies (e.g. Bastian et al. 2009; Scheepmaker et al. 2009). In this study, we apply the method to the resolved stellar population of a whole galaxy, following the prescription by Gouliermis, Hony & Klessen (2014). The innovation of our treatment lies in the use of the *deprojected* positions of the stars, eliminating the effect of projection on the measures of stellar pair separations. The constructed ACF is, thus, the true two-dimensional ACF of the galaxy, as if it was observed face-on. We determine the ACF of the stars from their deprojected coordinates as

$$1 + \xi(r) = \frac{1}{\bar{n} N} \sum_{i=1}^{N} n_i(r), \tag{2}$$

where N is the total number of stars, $n_i(r)$ is the number density of stars found in an aperture of radius r centred on star i and $\bar{n}$ is the average stellar number density. Uncertainties of this function are given by

$$\delta(1 + \xi(r)) = \sqrt{N} \cdot \left(\frac{1}{2} \sum_{i=1}^{N} n_{\rm p}(r) \right)^{-1/2}, \tag{3}$$

where $n_{\rm p}(r)$ is the number of pairs with the central star i of the current aperture, and the factor $1/2$ accounts for not counting every pair twice. The function $1 + \xi(r)$ is defined so that $\bar{n}[1 + \xi(r)]{\rm d}^2 r$ is the probability of finding a neighbouring star in an area of radius r from a random star in the sample. Therefore, for a random stellar distribution $1 + \xi(r) = 1$, while a truly clustered sample should have $1 + \xi(r) > 1$.

In a two-dimensional self-similar distribution, the total number of stars N within an aperture of radius r increases as $N \propto r^{D_2}$, where D_2 is the fractal dimension of the distribution (Mandelbrot 1983). Fractal distributions have a power-law dependence of the ACF with radius of the form $1 + \xi(r) \propto r^{\eta}$ (e.g. Larson 1995), which yields from equation (2) $N \propto r^{\eta} \cdot r^2 = r^{\eta + 2}$. The exponent η is thus related to the fractal dimension as $D_2 = \eta + 2$. For the derivation of the three-dimensional fractal dimension D_3 of a distribution, dedicated simulations are shown to be required (Gouliermis et al. 2014). The ACF is qualitatively an identical method to a power spectrum analysis. Both statistics are used in studies of cosmological large-scale structure (e.g. Szapudi et al. 2005) and of density structure in the turbulent interstellar matter (e.g. Federrath, Klessen & Schmidt 2009).

In Fig. 17, we show the ACF of the blue stellar sample observed in NGC 6503 (blue line). For comparison, we also show in red the ACF of the red stellar sample. It was possible to construct both functions for separations down to 0.75 arcsec, corresponding to physical scales of ∼20 pc. For smaller scales, there is an 'anti-correlation' of the ACF with separation, which drops rapidly towards the smallest separations. Apparently, photometric confusion dominates at scales smaller than 20 pc, a limit

[10] The velocity dispersion drop in NGC 6503 is also discussed by Bottema & Gerritsen (1997) and Puglielli et al. (2010).

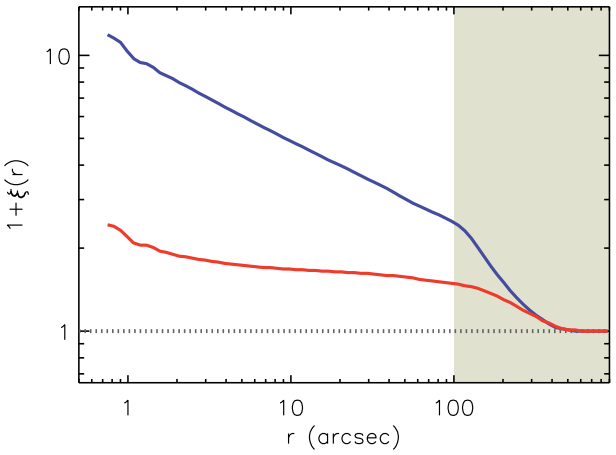

Figure 17. The two-point correlation (autocorrelation) function constructed for the two stellar samples of interest, revealed with LEGUS photometry in NGC 6503. The ACF of the young blue stellar population detected in *F*275*W* and *F*336*W* filters is shown with the blue line, while that of the older red stars selected in filters *F*555*W* and *F*814*W* is drawn with the red line. The grey flat dotted line represents the ACF of a uniformly distributed stellar population. From this plot it is shown that the young blue population follows a clustering behaviour, which is quite different from that of the evolved red stars, being *more clustered* than the latter. The ACF of the red stars, being almost flat, demonstrates that these stars are quite *more distributed* than the blue. The shaded area designates the length-scale, where the ACF calculation is unreliable – and thus not considered in our analysis – due to the edge effect introduced by the limited field of view.

which, thus, sets the resolution of our analysis with these data.[11] The ACF, being determined through the pair separations between all stars, can be calculated within a specific maximum length-scale limit, determined by the length of the unavoidably finite observed field of view. In practice, the continuously larger stellar pair separations calculated for each star in the sample eventually reach the edge of the observed field, beyond which there are no stars available for the calculation. If the ACF determination is not corrected for this edge effect, the calculation will be incorrect at large scales with its value dropping to the unrealistic $1 + \xi(r) < 1$.

We correct our calculations by masking the pair-separation measurements within the borders of the observed field of view, as prescribed by Gouliermis et al. (2014). This treatment corrects the stellar densities of equation (2) by using the true area surface constrained for the larger length-scales by the masking. This correction allows the ACF to fall smoothly to the limiting value of 1 at scales comparable to the edge of the observed field as shown in the plot of Fig. 17. In effect, the sharp drop to the limiting value of 1 sets the maximum length-scale within which the ACF is reliable. We denote in Fig. 17 with the greyed area the remaining unreliable length-scale range, which we do not take into account in our further analysis. It is interesting to note that the maximum scale, where a trustworthy ACF is calculated is $\simeq$100 arcsec ($\simeq$2.6 kpc), is far shorter than the complete extent of the deprojected field of view.

We determine the exponent η of the ACF through a linear regression on the log–log plots of Fig. 17 by applying a Levenberg–Marquardt non-linear least-squares minimization fit (Levenberg 1944; Marquardt 1963). In this figure, it is seen that both the blue and red stellar samples in NGC 6503 have a single-power-law stellar separation dependence of their ACF. The exponent η, however, is quite different between the two samples. The ACF of the young blue sample has a slope $\eta \simeq -0.30$, corresponding to a fractal dimension $D_2 = 1.7$. On the other hand, the ACF of the old red stellar sample is almost flat with $\eta \simeq -0.05$, i.e. $D_2 = 1.95$ (both slopes found with very small fitting errors).

There are two conclusions, connected to each other, one can derive from these results. (1) The steep monotonic ACF of the blue stars, corresponding to a fractal dimension much smaller than the geometrical dimension of 2, suggests a fractal, i.e. self-similar, distribution of young stars across NGC 6503. On the other hand, the flatter ACF for the red stars, with a fractal dimension very close to the geometric dimension, clearly implies a distribution for the old population, which is very well spread, almost equivalent to a uniform (random) spatial distribution.[12] (2) The absolute values for the ACF of the young stars, which are found systematically higher than those for the old stars at the same separation length, indicate the more 'clumpy' clustering behaviour of the former sample in comparison to the latter, with the young stars being systematically *more clustered* than the old.[13]

The steep ACF of the young stellar population in NGC 6503 demonstrates that these stars are hierarchically distributed across the whole measurable extent of the galaxy, up to scales $\sim$2.5 kpc. This implies that the hierarchical stellar structures identified in Section 2.3 are themselves part of an extended hierarchical distribution. Power laws similar to that found here for the ACF of young stars in NGC 6503 are derived from power spectra of interstellar gas over a large range of environments (e.g. Elmegreen & Elmegreen 2001), demonstrating the hierarchical morphology in the gas structure with a typical fractal dimension of $D_2 \simeq 1.5$ (Elmegreen et al. 2006).

4.3 Time evolution of stellar structural morphology

The sample of blue young stellar population of NGC 6503 includes stars of various ages, and therefore represents different star formation events within the recent star formation history of the galaxy. This is demonstrated in Fig. 18, where the colour–magnitude diagram (CMD) of the blue stars is shown with indicative stellar evolutionary models for solar metallicity from the Padova grid of models (Chen et al. 2015; see also Marigo et al. 2008; Girardi et al. 2010; Bressan et al. 2012). From the oldest isochrone, it can be derived that the stellar age limit covered by our blue photometric catalogue is $\gtrsim$100 Myr (red line in Fig. 18).

The stellar age range covered in our sample allows us to address the question whether star formation is a purely clustered process, or stars are also frequently born in a distributed fashion over galactic scales by investigating the clustering behaviour of young stars at

[11] Spatial scales <20 pc, corresponding to the cluster-formation regime, will be addressed with the star clusters census of NGC 6503, which is currently under construction (Adamo et al., in preparation).

[12] The derived value for the ACF of the red population serves as a confirmation of the capability of the method to distinguish a randomly dispersed sample of stars from any other distribution (fractal or not), by its flat ACF, which corresponds to a fractal dimension comparable to its geometrical one (see e.g. Gouliermis et al. 2014, for comparisons with the ACF of synthetic fractal and centrally condensed distributions).

[13] The clumpy clustering of the young stars is tightly connected to their self-similar distribution. The more fractal a distribution is, i.e. with lower D_2 values, the more prominent sub-clustering behaviour its stars have, i.e. higher ACF values (Gouliermis et al. 2014).

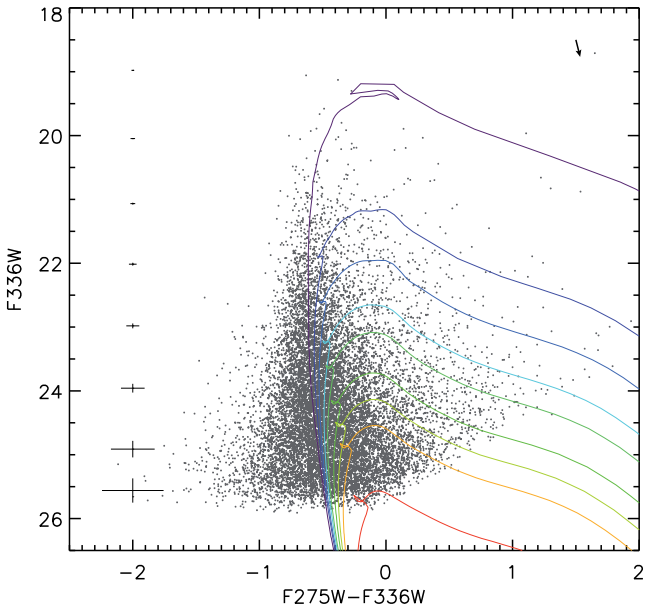

Figure 18. Total *F*275*W*, *F*336*W* CMD of the blue stars detected in NGC 6503 with our photometry, with indicative isochrones from the Padova family of evolutionary models overlaid. Indicative isochrone models corresponding to stellar ages between 4 Myr (purple line) and 110 Myr (red line) are shown. The crosses on the left represent typical uncertainties in brightness and colour in our photometry. Isochrones are chosen for solar metallicity, and they are corrected for distance (with a distance modulus 28.6 mag) and foreground extinction, represented by the arrow on the top right of the diagram, according to the reddening law by Fitzpatrick (1999). Only the MS and sub-giant branch are shown for each of the models for clarity. This plot demonstrates the dynamic range in stellar ages covered by our photometry.

sequential evolutionary stages. The ACF treatment described in the previous section for the characterization of the clustering behaviour of the whole blue sample can also be applied to stars of different ages. The construction of the ACF for sub-samples of different ages would thus provide an assessment of how the clustering behaviour of young populations evolves with time across the whole galaxy, over the last ∼100 Myr, as investigated for example in the Magellanic Clouds (Gieles et al. 2008; Bastian et al. 2009).

The derivation of ages of blue bright stars from their photometry alone is a complicated process and implies significant uncertainties for the derived parameters, even with the use of multi-band photometric measurements. In order, thus, to retain most of the original information derived from our catalogues, and to avoid introducing model-dependent uncertainties, we group the sample of blue stars in ranges defined by their magnitudes in the *F*336*W* filter. We use this selection as a proxy for dividing the stars into groups of different evolutionary stages. In CMDs as that of Fig. 18, both the turn-off (TO) and the He burning, starting immediately after the TO, correspond for every isochrone to a specific *F*336*W* magnitude which for older stars is systematically fainter. As a consequence, following the analysis by, e.g., Bastian et al. (2009), we group the stars within continuously fainter magnitude bins in order to roughly divide them into age bins. It should be noted that while the brightest magnitude range is populated only by the youngest stars, fainter ranges should also include stars younger than the corresponding age limit. We assess, however, that the fraction of younger contaminants is small enough not to significantly affect the canonical age of each magnitude bin.[14]

4.3.1 *Two-point correlation functions*

The blue stellar catalogue is divided into eight magnitude bins, all containing equal numbers of ≃1600 stars. Dividing the catalogue into ranges of equal numbers satisfies equivalent statistical significance among all sub-samples. The limiting magnitudes of each sub-sample are shown in the first column of Table 4. The corresponding limiting age and stellar mass for each sub-sample, defined by the TO of the corresponding isochrone, are given in the second and third columns of the table, respectively. We construct the ACF for each of the blue sub-samples. The ACFs are shown in Fig. 19 and the corresponding ACF exponent η is given in column 4 of Table 4. Since some of the ACFs show broken power-law shapes, while others do not, we estimate η up to the scalelength where all ACFs remain unchanged (for scales ≃20 arcsec). From this analysis, we find that indeed the brighter (and younger) stars in our sample are more clustered than the fainter ones. This is demonstrated by both their systematically higher ACF values and steeper ACF slopes, which correspond to smaller D_2 and, thus, more clumpy distributions.

The analysis described above also helps us designate the timescale, where a significant change in the clustering behaviour of stars occurs. Specifically, η for the three brightest magnitude intervals is quite different from one range to the other and from the remaining faint magnitude ranges. Specifically, η becomes systematically shallower for stars with indicative ages between $\lesssim$30 Myr and ∼50 or 60 Myr with values between ∼−0.7 and ∼−0.3. However, from this age on η remains almost unchanged with the value of ∼−0.2 up to ∼110 Myr. This result implies that while structure in the morphology of stellar clustering survives for the whole considered age range of $\lesssim$100 Myr, it changes significantly its behaviour within the first ∼60 Myr. It is also interesting to note that according to the ACF slopes found here, the clustering behaviour of stars at the age limits ∼50–60 Myr defines the behaviour of the whole sample the ACF of which has similar slope ($\eta \sim -0.3$; Section 4.2). The fitting uncertainty of the ACF exponent, η, is typically very small, ranging from less than 0.01 for stars in the brighter sub-sample up to ∼0.03 for those in the fainter sub-sample. The measured errors are also given in column 4 of Table 4.

4.3.2 *Pair and MST separations*

According to the results above, since younger stars show a more clumpy clustering behaviour than the older, they should also be typically confined in smaller length-scales. We confirm this result with the application of two measurements, the probability distribution function (PDF) of pair separations of all stars in each sub-sample and the corresponding *MST* of these stars.

We calculate the PDF of pair separations for all stars in each sample, as the sum of the probability functions of the stars, determined by the number of pair separations that fall in given separation bins

[14] For a constant star formation rate, a 100 Myr old blue population and a disc of ∼10 Gyr, the young part in the fainter magnitude bins does not exceed ∼1 per cent of the old part.

Table 4. Measures of the clustering behaviour of young stars in eight distinct magnitude ranges, corresponding roughly to different stellar age intervals between ∼4 and 110 Myr. Magnitudes, ages and masses listed in the first three columns correspond to the upper limits of each interval. The results of three different measurements are given: the ACF slope η (column 4); the median of all pair separations among stars in every sub-sample (columns 5 and 6); the median MST edge length among stars in each sub-sample (columns 7 and 8). All measures indicate that the typical length-scale of stellar clustering depends on the brightness (age) range of the stars, with the brighter (younger) being concentrated in systematically smaller scales.

m_{336} limit	Age (Myr)	Mass ($M_\odot$)	η	Pair sep. median (arcsec)	(kpc)	MST median (arcsec)	(pc)
22.97	32	8.8	-0.693 ± 0.004	77.3	1.99	1.41	36.4
23.62	40	7.7	-0.470 ± 0.007	80.2	2.06	1.85	47.6
24.06	50	6.9	-0.321 ± 0.009	80.0	2.06	1.89	48.7
24.41	63	6.2	-0.289 ± 0.011	82.4	2.12	2.04	52.4
24.72	71	5.9	-0.232 ± 0.012	81.9	2.11	2.19	56.4
25.01	89	5.3	-0.233 ± 0.015	84.5	2.17	2.33	60.0
25.30	100	5.1	-0.225 ± 0.016	87.9	2.26	2.33	59.8
25.91	112	4.9	-0.204 ± 0.031	104.9	2.70	2.96	76.0

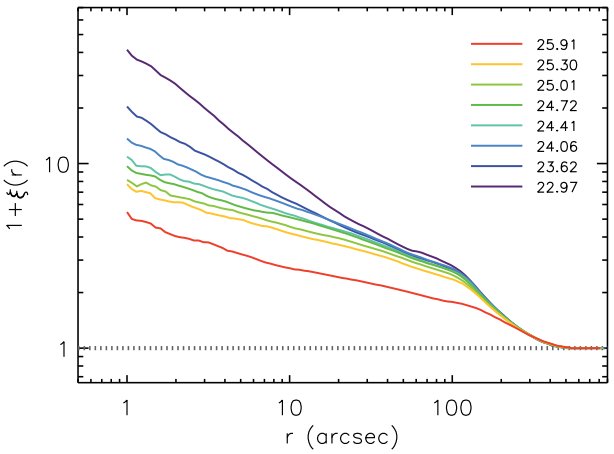

Figure 19. The two-point correlation (autocorrelation) function constructed for eight selected equally numbered sub-groups of our sample of blue stars, corresponding to different magnitude intervals. In the plot legend, the limit of each magnitude bin in the *F*336*W* filter is given next to the corresponding colour line.

around each star (e.g. Cartwright & Whitworth 2004):

$$p(r_j) = \sum_{i=1}^{N} \frac{2\,N_{ij}}{N\,(N-1)\,\mathrm{d}r}\,. \qquad (4)$$

In this function N is the total number of stars, N_{ij} is the number of pair separations that fall in the separation bin centred on r_j around star i and dr is the width of each separation bin. The probability that the projected separation between two randomly chosen stars is in the interval (r, r + dr) is given by $p(r)$dr. The constructed pair-separation PDFs of young stars show different maxima for different magnitude ranges. Specifically, the PDF becomes systematically more truncated towards smaller separations and its peak occurs at smaller length-scales for stars in younger sub-samples. The median of each derived PDF is given in arcsec and kpc in columns 5 and 6 of Table 4, respectively. While the rms dispersion in each PDF is large enough to cover the median of its neighbouring PDFs, these values show a clear trend of the typical pair separation of stars towards smaller lengths for higher stellar brightness and age.

The MST, a construct from graph theory, is defined as the unique set of straight lines, called 'edges', connecting a given set of points without closed loops, such that the sum of the edge lengths is the minimum (e.g. Kruskal 1956; Prim 1957). This method has been broadly used, along with other techniques, in clustering analysis of stellar samples (see e.g. Schmeja 2011, for a review). Here, we construct the PDF of the edge lengths among stars in every sub-sample, as we did for their pair separations, as defined in equation (4). In this measurement instead of the pair separations among all stars, we consider the separations (edge lengths) of each star from its nearest neighbours, as determined by the MST. The median of the MST edge lengths for each stellar sample is given in arcsec and parsec in columns 7 and 8, respectively, of Table 4. Again, there is a clear trend of younger stars being systematically clumped in smaller scales as defined by the MST.

The similarity of the scaling relations over stellar age found with both methods is demonstrated in Fig. 20, where the corresponding medians are plotted with respect to the limiting magnitude and the equivalent age limit of each stellar sub-sample. Typical uncertainties for the medians, corresponding to a few per cent, are also shown in Fig. 20. They are calculated from the values corresponding to the data positions around the median within the Poisson dispersion of its position.

While both measurements show the same trend of scale with age, the difference in the results between the pair separations and MST edge lengths, which reflects the difference of almost two orders of magnitude between the corresponding medians, lies on the fact that while the PDF of the pair separations is constructed from the whole extent of separations up to the highest covered length-scales, that of the MST edge length considers only the shortest edges between each star and its neighbours. Under these circumstances, the medians given in Table 4 for the MST edge lengths represent the most likely typical scale of clustering for each stellar sample, while those for the pair separations correspond to the complete extent where stars in each magnitude bin are located over the whole observed field of view of the galaxy. The pair-separation medians provide, thus, the 'inter-structure' scalelength of stars at different ages, beyond the 'typical' stellar clusterings, determined by the MST.

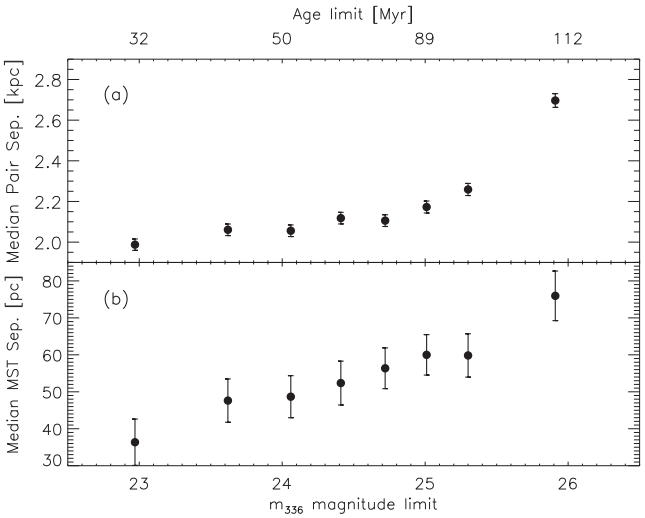

Figure 20. Relation between the medians of (a) the pair stellar separations and (b) the MST edge lengths and the limiting magnitude (or age) for stars in eight selected brightness ranges (corresponding to different age intervals). These plots demonstrate that there is a dependence of the clustering length-scales of stars on their age.

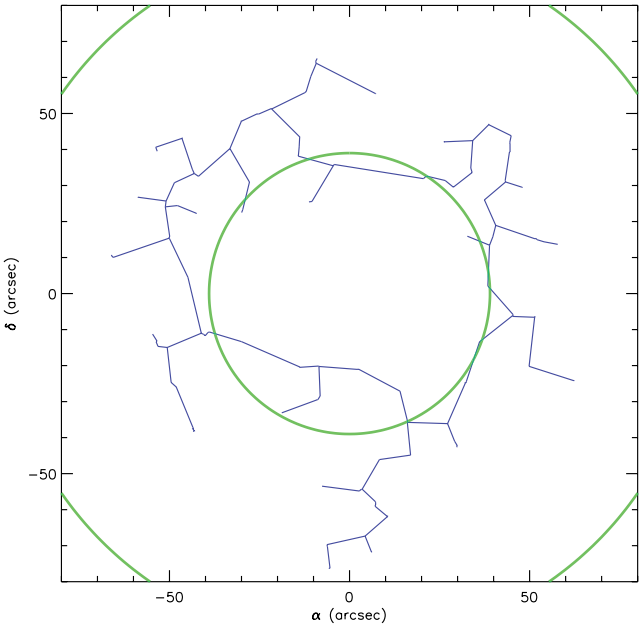

Figure 21. MST connecting the positions of young stellar structures detected at significance levels higher than 3σ (blue line). The MST connects each object to its nearest neighbour, drawing thus the positional alignment of these structures with respect to the star-forming ring borders shown with the green circles.

5 DISCUSSION

The multi-scale sample of young stellar structures detected in NGC 6503 suggests that star formation over a period of ∼100 Myr takes place within the typical scale of few hundred parsecs (Section 3.1) in structures, which are themselves hierarchical as shown from their dendrogram (Section 3.2). The self-similar distribution of all young stars across the galaxy, demonstrated by their ACF, implies that hierarchical structure in the stellar distribution occurs not only inside but also beyond the borders of these structures. Therefore, one can conclude that all star-forming structures are connected to each other in a hierarchical fashion through their coexistence in the star-forming ring of the galaxy (identified in Section 4.1).

Hierarchical structural morphology in stellar ensembles has been found by Elmegreen et al. (2014) in the UV images of 12 LEGUS galaxies (NGC 6503 not included in the sample) over a length-scale range of ∼1–200 pc. The power-law length-scale correlations in the size and flux distribution functions of nested star-forming regions suggest that hierarchically structured star-forming regions with sizes of few hundred parsecs represent common unit structures. This is in line with our findings concerning the typical length-scale of the identified young stellar structures in NGC 6503. Hierarchical structure was identified by Elmegreen et al. (2014) only inside and not among the different star-forming patches, in both large spiral galaxies and low surface brightness dwarfs, as well as in starburst dwarfs or H II galaxies, which are dominated by one or two large star-forming regions. In the case of NGC 6503, self-similar stellar distributions are also detected among the star-forming structures, suggesting that they are all connected to each other in a hierarchical fashion within the dominant star-forming ring of the galaxy.

The observed hierarchical structure of star-forming complexes in NGC 6503 and other galaxies is consistent with the model where star formation is regulated by turbulence, via, e.g. *turbulent fragmentation*, i.e. gas compressions that form successively smaller clouds inside larger ones (Vázquez-Semadeni et al. 2009). Such processes form a similar hierarchy of young stars, with a likely secondary correlation for star age, making larger regions older in proportion to the turbulent crossing time (Efremov & Elmegreen 1998; de la Fuente Marcos & de la Fuente Marcos 2009). Our findings for stars in different evolutionary stages confirm this time-length correlation, with younger stars being confined in smaller length-scale than the older. The hierarchy in stellar structures has an upper limit in size beyond which separate regions form independently (Elmegreen et al. 2014). In the case of NGC 6503, this limit is set by the size of the star-forming ring of the galaxy. This is consistent with the observation that the two-point correlation for stars decreases as a power law with increasing scale up to about 2.5 kpc.

The peak observed in the young stellar surface density profile of Fig. 16 corresponds to the star-forming ring of the galaxy, and thus its wings define the radial limits of the ring. These limits suggest an inner radius of ∼1 kpc and an outer radius of ∼2.5 kpc. We derive from the stellar rotational curve of NGC 6503 (Bottema 1989) the projected asymptotic circular velocity for these radii to be of the order of ∼110 km s^{-1} at the outer ring radius and ∼80 km s^{-1} at the inner, corresponding to rotational velocities $\Omega_{\rm out} \simeq 1.4 \times 10^{-15}$ rad s^{-1} and $\Omega_{\rm inn} \simeq 2.6 \times 10^{-15}$ rad s^{-1}, respectively. The rotational velocity difference between the edges of the ring of about 10^{-15} rad s^{-1} is comparable to the pattern speed of Milky Way's spiral arms (Bissantz, Englmaier & Gerhard 2003). It most probably introduces a shear that should influence strongly the star formation process across it.

This shear within ∼100 Myr, which is the time covered by our observed young stellar sample, would have stretched a single compact object inwards, providing that this object is dense enough to survive. The surface stellar density maps of Figs 7 and 8 suggest an alignment of the detected young stellar structures across the ring of NGC 6503. This trend is visualized by the MST of all structures found at significance levels $\geq 3\sigma$, shown in Fig. 21. In this figure, the connecting edge lengths show an alignment that both

follows and traverses the ring closer to its inner part. Considering that the ring has performed several rotations during the last 100 Myr,[15] it stands to reason that shear functions more as a supportive rather than destructive factor to star formation. The observed clustering of young stars in NGC 6503 can thus be interpreted as being induced by turbulence, the driving source for which is probably gravitational instabilities induced by shear, with larger structures becoming spiral-like (flocculent) because of their longer dynamical time-scales in comparison to the shear time (e.g. Elmegreen 2011).

6 SUMMARY

We present a detailed clustering analysis of the young blue stellar population identified with LEGUS across the star-forming ring galaxy NGC 6503. We construct stellar surface density maps and apply a contour-based analysis technique to identify the stellar complexes' population of the galaxy. We identify 244 distinct structures at various stellar density (significance) levels. We organize these structures into 82 separate groups, according to their association with a single low-density parental structure. These groups are arranged into eight families of structures, corresponding to eight super-structures, determined by the 1σ isopleths. Three of these super-complexes contain 95 per cent of the structures. The hierarchical classification of structures into groups and families, according to their membership to larger and sparser stellar constellations, is illustrated by their *dendrogram* or *structure tree*.

We determine structural parameters, i.e. size, stellar density and total brightness, for each structure. The sizes of the detected systems average around ∼130 (±40) pc, a length-scale comparable to but still larger than ∼80 pc, the scale which is discussed as a characteristic galactic scale for star formation (see e.g. Gouliermis 2011, and references therein). About 60 per cent of the observed young stellar population is found to belong to one of the 1σ super-structures, suggesting that ∼40 per cent of the young blue stars are distributed in an 'unclustered' fashion inside the star-forming ring. The first statistically significant sample of stellar concentrations, detected at the 3σ density level, accounts for only 34 per cent of the total observed young stellar content, increasing the remaining fraction of 'unclustered' young stars to 66 per cent.

On average, the size (and its dispersion), the total UV brightness and the fraction of included young stars show a dependence on the density level where the corresponding structures are detected. The fraction of UV light included in the structures over the total observed stellar UV emission shows a steeper dependence on density than that of the stellar fraction. This difference, which becomes more important for higher densities, suggests that compact stellar structures, identified at higher density levels, encompass on average the UV-brightest stars in the galaxy.

We identify a power-law mass–size relation, determined by the correlation between radius and number of stars. The exponent of this relation for all structures is less than 2 as expected for a fractal distribution of stars (e.g. Elmegreen & Falgarone 1996). Our findings suggest a dependence of the power-law index of the mass–size relation on the detection threshold, in agreement with previous studies in the Large Magellanic Cloud (Gouliermis et al. 2003) and M33 (Bastian et al. 2007). A correlation between the volume stellar density and the size of the structures was also found. This relation for the systems detected at 5σ and 6σ levels resembles Larson's third relation (Larson 1981) and becomes steeper for higher density structures, possibly reflecting their steeper density profiles. Since the volume density scales inversely with size, the identified correlation implies a dependence of the parameter determination for the structures on the detection criteria, in a similar manner as for GMCs.

The radial surface density profile of the young stars in NGC 6503 shows a very strong central peak and drops rapidly within a radial distance of ∼350 pc, in agreement with the line-of-sight velocity dispersion profile, which shows a sharp decrease within 300 pc (Bottema 1989; Bottema & Gerritsen 1997). The stellar density profile rises again and reaches its peak at a distance of ∼1.9 kpc, after which drops again exponentially. This profile, demonstrating a circumnuclear deficiency in young stars, agrees with both an inner truncated disc and a ring being formed by a bar (Puglielli et al. 2010). The confinement, though, of all young stellar structures in a ring-shaped alignment favours the ring-formation scenario, as earlier suggested (Freeland et al. 2010).

We characterize the hierarchy in the global clustering behaviour of young stars across NGC 6503 with the ACF. We find that the ACF of these stars shows the typical features of a self-similar stellar distribution with a two-dimensional fractal dimension $D_2 = 1.7$. The observed hierarchy in young stellar clustering extends monotonically across the complete measurable dynamic range in length-scales of two orders of magnitude (∼20–2500 pc). The self-similar distribution of young stars across NGC 6503 is consistent with the hierarchical morphology of the star-forming complexes of the galaxy, and the mass–size relation of the structures, which fits to the expectations for fractal clusterings.

We investigate the clustering behaviour of young stars at different evolutionary stages with the ACF of stars in different magnitude intervals. We find that younger (brighter) stars are more clustered than the older. The ACF exponents of the younger stars are systematically higher, corresponding to smaller fractal dimensions and more clumpy distributions, than those for the older stars. This analysis shows that the time-scale, where a significant change from a more clustered to a more distributed assembling of stars takes place, is about 60 Myr. A similar trend was found for the Small and Large Magellanic Clouds, with a time-scale for substructure evolution towards a uniform distribution of ∼75 and 175 Myr, respectively (Gieles et al. 2008; Bastian et al. 2009). Larger scale occupancy by stars of decreasing luminosity is previously discussed also for the spiral NGC 1313 and dwarf irregular IC 2574 (Pellerin et al. 2007, 2012). These results are confirmed with the pair separations and MST edge-length probability distributions of the stars in the various magnitude (age) ranges.

Based on kinematic arguments, we assess that hierarchy in the young stellar clustering in NGC 6503 is probably induced by turbulence, driven by shear in the ring of the galaxy. With this mechanism, large stellar structures become *flocculent* because their dynamical time-scales exceed the shear time.

ACKNOWLEDGEMENTS

DAG kindly acknowledges financial support by the German Research Foundation (DFG) through grant GO 1659/3-2. This research has made use of the NASA/IPAC Extragalactic Database (NED), which is operated by the Jet Propulsion Laboratory, California Institute of Technology, under contract with the

[15] A fit to the stellar rotational curve of NGC 6503 (Bottema 1989), based on the fitting formula by Courteau (1997), yields a projected asymptotic circular velocity of 108 ± 4 km s^{-1}, and a projected length-scale of 0.95 ± 0.04 kpc (Puglielli et al. 2010), suggesting that the inner part of the ring has performed more than three full rotations during the last 100 Myr.

National Aeronautics and Space Administration. This research has also made use of the SIMBAD data base, operated at CDS, Strasbourg, France. Based on observations made with the NASA/ESA *Hubble Space Telescope*, obtained from the data archive at the Space Telescope Science Institute (STScI). STScI is operated by the Association of Universities for Research in Astronomy, Inc. under NASA contract NAS 5-26555. These observations are associated with programme GO-13364. Support for programme 13364 was provided by NASA through grants from STScI. This research made use of the TOPCAT[16] application (Taylor 2005), and NASA's Astrophysics Data System (ADS) bibliographic services.[17]

REFERENCES

Bastian N., Ercolano B., Gieles M., Rosolowsky E., Scheepmaker R. A., Gutermuth R., Efremov Yu., 2007, MNRAS, 379, 1302
Bastian N., Gieles M., Ercolano B., Gutermuth R., 2009, MNRAS, 392, 868
Baugh C., Murdin P., 2000, Encyclopedia of Astronomy and Astrophysics. IoP Publishing, Bristol
Bissantz N., Englmaier P., Gerhard O., 2003, MNRAS, 340, 949
Bolatto A. D., Leroy A. K., Rosolowsky E., Walter F., Blitz L., 2008, ApJ, 686, 948
Bottema R., 1989, A&A, 221, 236
Bottema R., Gerritsen J. P. E., 1997, MNRAS, 290, 585
Bressan A., Marigo P., Girardi L., Salasnich B., Dal Cero C., Rubele S., Nanni A., 2012, MNRAS, 427, 127
Buta R., Combes F., 1996, Fundam. Cosm. Phys., 17, 95
Buta R. J. et al., 2015, ApJS, 217, 32
Calzetti D. et al., 2015, AJ, 149, 51
Carpenter J. M., 2000, AJ, 120, 3139
Cartwright A., Whitworth A. P., 2004, MNRAS, 348, 589
Chen Y., Bressan A., Girardi L., Marigo P., Kong X., Lanza A., 2015, MNRAS, in press
Comerón S., Knapen J. H., Beckman J. E., 2008, A&A, 485, 695
Courteau S., 1997, AJ, 114, 2402
Cox A. N., 2000, Allen's Astrophysical Quantities, 4th edn. Springer-Verlag, New York
Dale D. A. et al., 2009, ApJ, 703, 517
de la Fuente Marcos R., de la Fuente Marcos C., 2009, ApJ, 700, 436
de Lorenzo-Cáceres A., Falcón-Barroso J., Vazdekis A., Martínez-Valpuesta I., 2008, ApJ, 684, L83
de Vaucouleurs G., de Vaucouleurs A., Corwin H. G., Jr Buta R. J., Paturel G., Fouqué P., 1991, Third Reference Catalogue of Bright Galaxies, Vols I–III. Springer-Verlag, New York
Dolphin A. E., 2000, PASP, 112, 1383
Efremov Y. N., Elmegreen B. G., 1998, MNRAS, 299, 588
Efremov I. N., Ivanov G. R., Nikolov N. S., 1987, Ap&SS, 135, 119
Elmegreen B. G., 2011, EAS Publ. Ser., 51, 31
Elmegreen B. G., Elmegreen D. M., 2001, AJ, 121, 1507
Elmegreen B. G., Falgarone E., 1996, ApJ, 471, 816
Elmegreen B. G., Efremov Y., Pudritz R. E., Zinnecker H., 2000, in Mannings V., Boss A. P., Russell S. S., eds, Protostars and Planets IV. University of Arizona Press, Tucson, p. 179
Elmegreen B. G., Elmegreen D. M., Chandar R., Whitmore B., Regan M., 2006, ApJ, 644, 879
Elmegreen D. M. et al., 2014, ApJ, 787, L15
Federrath C., Klessen R. S., Schmidt W., 2009, ApJ, 692, 364
Fitzpatrick E. L., 1999, PASP, 111, 63
Freeland E., Chomiuk L., Keenan R., Nelson T., 2010, AJ, 139, 865
Freeman K. C., 1970, ApJ, 160, 811
Gieles M., Bastian N., Ercolano B., 2008, MNRAS, 391, L93
Girardi L. et al., 2010, ApJ, 724, 1030
Gomez M., Hartmann L., Kenyon S. J., Hewett R., 1993, AJ, 105, 1927
Gouliermis D. A., 2011, Phys. Scr., 84, 048401
Gouliermis D., Kontizas M., Korakitis R., Morgan D. H., Kontizas E., Dapergolas A., 2000, AJ, 119, 1737
Gouliermis D., Kontizas M., Kontizas E., Korakitis R., 2003, A&A, 405, 111
Gouliermis D. A., Schmeja S., Klessen R. S., de Blok W. J. G., Walter F., 2010, ApJ, 725, 1717
Gouliermis D. A., Hony S., Klessen R. S., 2014, MNRAS, 439, 3775
Greisen E. W., Spekkens K., van Moorsel G. A., 2009, AJ, 137, 4718
Heyer M., Krawczyk C., Duval J., Jackson J. M., 2009, ApJ, 699, 1092
Houlahan P., Scalo J., 1992, ApJ, 393, 172
Ivanov G. R., 1996, A&A, 305, 708
Karachentsev I. D. et al., 2003, A&A, 398, 479
Kauffmann J., Pillai T., Shetty R., Myers P. C., Goodman A. A., 2010a, ApJ, 712, 1137
Kauffmann J., Pillai T., Shetty R., Myers P. C., Goodman A. A., 2010b, ApJ, 716, 433
Knapen J. H., Mazzuca L. M., Böker T., Shlosman I., Colina L., Combes F., Axon D. J., 2006, A&A, 448, 489
Kormendy J., 1977, ApJ, 217, 406
Kruskal J. B., Jr, 1956, Proc. Am. Math. Soc., 7, 48
Kuzio de Naray R., Arsenault C. A., Spekkens K., Spekkens K., Sellwood J. A., McDonald M., Simon J. D., Teuben P., 2012, MNRAS, 427, 2523
Larson R. B., 1981, MNRAS, 194, 809
Larson R. B., 1995, MNRAS, 272, 213
Levenberg K., 1944, Q. Appl. Math., 2, 164
Lira P., Johnson R. A., Lawrence A., Cid Fernandes R., 2007, MNRAS, 382, 1552
MacArthur L. A., Courteau S., Holtzman J. A., 2003, ApJ, 582, 689
Mandelbrot B. B., 1983, The Fractal Geometry of Nature. Freeman & Co., San Francisco
Maragoudaki F., Kontizas M., Kontizas E., Dapergolas A., Morgan D. H., 1998, A&A, 338, L29
Marigo P., Girardi L., Bressan A., Groenewegen M. A. T., Silva L., Granato G. L., 2008, A&A, 482, 883
Marquardt D., 1963, SIAM J. Appl. Math., 11, 431
Mazzuca L. M., Knapen J. H., Veilleux S., Regan M. W., 2008, ApJS, 174, 337
Myers P. C., 1983, ApJ, 270, 105
Peebles P. J. E., 1980, The Large-Scale Structure of the Universe. Princeton Univ. Press, Princeton, NJ, p. 435
Pellerin A., Meyer M., Harris J., Calzetti D., 2007, ApJ, 658, L87
Pellerin A., Meyer M. M., Calzetti D., Harris J., 2012, AJ, 144, 182
Prim R. C., 1957, Bell Syst. Tech. J., 36, 1389
Puglielli D., Widrow L. M., Courteau S., 2010, ApJ, 715, 1152
Román-Zúñiga C. G., Elston R., Ferreira B., Lada E. A., 2008, ApJ, 672, 861
Rosolowsky E. W., Pineda J. E., Kauffmann J., Goodman A. A., 2008, ApJ, 679, 1338
Scheepmaker R. A., Lamers H. J. G. L. M., Anders P., Larsen S. S., 2009, A&A, 494, 81
Schlafly E. F., Finkbeiner D. P., 2011, ApJ, 737, 103
Schmeja S., 2011, Astron. Nachr., 332, 172
Schmeja S., Klessen R. S., 2006, A&A, 449, 151
Schwarz M. P., 1984, MNRAS, 209, 93
Simkin S. M., Su H. J., Schwarz M. P., 1980, ApJ, 237, 404
Solomon P. M., Rivolo A. R., Barrett J., Yahil A., 1987, ApJ, 319, 730
Szapudi I., Pan J., Prunet S., Budavári T., 2005, ApJ, 631, L1
Taylor M. B., 2005, in Shopbell P., Britton M., Ebert R., eds, ASP Conf. Ser. Vol. 347, Astronomical Data Analysis Software and Systems XIV. Astron. Soc. Pac., San Francisco, p. 29
Tielens A. G. G. M., 2005, The Physics and Chemistry of the Interstellar Medium. Cambridge Univ. Press, Cambridge, UK
Vázquez-Semadeni E., Gómez G. C., Jappsen A.-K., Ballesteros-Paredes J., Klessen R. S., 2009, ApJ, 707, 1023
Wozniak H., Combes F., Emsellem E., Friedli D., 2003, A&A, 409, 469

[16] TOPCAT is available at the permalink http://www.starlink.ac.uk/topcat/
[17] Accessible at http://adswww.harvard.edu/ and http://cdsads.u-strasbg.fr/

SUPPORTING INFORMATION

Additional Supporting Information may be found in the online version of this paper:

Table 2. Survey of the young stellar structures in NGC 6503. Explanations on the characteristic parameters of the structures are given in the text (Section 3.1) (http://mnras.oxfordjournals.org/lookup/suppl/doi:10.1093/mnras/stv1325/-/DC1).

Please note: Oxford University Press are not responsible for the content or functionality of any supporting materials supplied by the authors. Any queries (other than missing material) should be directed to the corresponding author for the paper.

[1]*Institute for Theoretical Astrophysics, Centre for Astronomy, University of Heidelberg, Albert-Ueberle-Str. 2, D-69120 Heidelberg, Germany*
[2]*Max Planck Institute for Astronomy, Königstuhl 17, D-69117 Heidelberg, Germany*
[3]*Department of Physics and Astronomy, Johns Hopkins University, 3701 San Martin Drive, Baltimore, MD 21218, USA*
[4]*IBM Research Division, T.J. Watson Research Center, Yorktown Hts., NY 10598, USA*
[5]*Department of Physics and Astronomy, Vassar College, Poughkeepsie, NY 12604, USA*
[6]*Department of Astronomy, University of Massachusetts – Amherst, Amherst, MA 01003, USA*
[7]*Space Telescope Science Institute, 3700 San Martin Drive, Baltimore, MD 21218, USA*
[8]*Department of Astronomy, Oskar Klein Centre, Stockholm University, AlbaNova University Centre, SE-106 91 Stockholm, Sweden*
[9]*Department of Physics and Astronomy, University of Wyoming, Laramie, WY 82071, USA*
[10]*Department of Astronomy, University of Wisconsin-Madison, WI 53706, USA*
[11]*Astronomisches Rechen-Institut, Zentrum für Astronomie der Universität Heidelberg, Mönchhofstr. 12-14, D-69120 Heidelberg, Germany*
[12]*Instituto de Astrofsica de Canarias, Research Division, C/ Vía Láctea s/n, E-38200 La Laguna, Tenerife, Spain*
[13]*Lowell Observatory, 1400 West Mars Hill Road, Flagstaff, AZ 86001, USA*
[14]*Department of Astronomy, University of Virginia, PO Box 400325, Charlottesville, VA 22904-4325, USA*
[15]*School of Earth and Space Exploration, Arizona State University, Tempe, AZ 85287, USA*
[16]*Korea Astronomy and Space Science Institute, 305-348 Daejeon, Republic of Korea*
[17]*Department of Physics and Astronomy, University of Alabama, Tuscaloosa, AL 35487-0324, USA*
[18]*Department of Physics and Astronomy, State University of New York at Geneseo, Geneseo, NY 14454, USA*
[19]*Department of Physics and Astronomy, Bologna University, I-40127 Bologna, Italy*
[20]*INAF-Osservatorio Astronomico di Bologna, Via Ranzani 1, I-40127 Bologna, Italy*
[21]*European Space Agency and Space Telescope Science Institute, 3700 San Martin Drive, Baltimore, MD 21218, USA*

This paper has been typeset from a TEX/LATEX file prepared by the author.